Supporting Information

Reconfiguring Zn Deposition Dynamics via Epitaxial Zn^{2+} Pathway in Profiled Viscose Rayon for Long-Cyclability Zinc-Ion Batteries

Sainan Ou,[a,†] Jiaxian Zheng[a,†], Xingshu Chen,[a] Ran Li,[a] Zhanhui Yuan,*[a] Shude Liu,*[b] Yao Niu,[c] Meng An,*[d] Ge Zhou,[e] Yusuke Yamauchi,[f,g,h] Xinxiang Zhang*[a]

[a]College of Materials Engineering, Fujian Agriculture and Forestry University, Fuzhou, 350108, China

E-mail: zhanhuiyuan@fafu.edu.cn (Z. Yuan); xxzhang0106@fafu.edu.cn (X. Zhang)

[b]Engineering Research Center of Technical Textiles, Ministry of Education, College of Textiles, Donghua University, Shanghai, 201620, China

E-mail: sdliu@dhu.edu.cn

[c]College of Mechanical and Electrical Engineering, Shaanxi University of Science and Technology, Xi'an, 710021, China

[d]Department of Mechanical Engineering, The University of Tokyo, 7-3-1 Hongo, Bunkyo, Tokyo 113-8656, Japan

E-mail: anmeng@photon.t.u-tokyo.ac.jp (M. An)

[e]College of Chemistry, Sichuan University, Chengdu, 610040, China

[f]School of Chemical Engineering and Australian Institute for Bioengineering and Nanotechnology (AIBN), The University of Queensland, Brisbane, QLD 4072, Australia

[g]Department of Materials Process Engineering, Graduate School of Engineering, Nagoya University, Nagoya 464-8603, Japan

[h]Department of Chemical and Biomolecular Engineering, Yonsei University, 50 Yonsei-ro, Seodaemun-gu, Seoul 03722, South Korea

[†] These authors contribute equally to this work.

1. Experimental Section

1.1 Materials

The 100% cotton spunlaced non-woven fabric (named CF, 20 cm × 15 cm) was acquired from Huangkai Brand Management Co., Ltd (Hunan, China). Spunlace non-woven fabric with 50% polyester fiber and 50% viscose rayon (named BF, 20 cm×15 cm) was purchased from Yixiang Health Technology Co., Ltd (Henan, China). The 100% viscose spunlaced non-woven fabric (named VF, 20 cm×15 cm) was obtained from Keer Cosmetics Co., Ltd (Zhejiang, China). Glass fiber (named GF, model: 1823-047) was attained from the Whatman Co., Ltd. Filter paper (named FP) was bought from Special Paper Industry Co., Ltd (Hangzhou, China).

Zn foil (thickness, 0.1 mm; purity, 99.995%) was obtained from Wenghe Metal Materials Co., Ltd (Hefei, China). Stainless steel foil (thickness, 0.01 mm) was obtained from Jingtian Stainless Steel Products Co., Ltd (Taizhou, China). Copper foil (thickness, 9 μm) and button cell shells were procured from Yajun Battery Materials Co., Ltd (Taizhou, China).

$ZnSO_4·7H_2O$ (AR), $MnSO_4·H_2O$ (AR, 99%), polyvinylidene fluoride (PVDF) and N-methylpyrrolidone (NMP, 99.9%) were all bought from Aladin Biochemical Technology Co., Ltd (Shanghai, China). $C_2H_2O_4·2H_2O$ (AR) and NH_4VO_3 (AR) were purchased from Sinopharm Chemical Reagent Co., Ltd (Shanghai, China).

1.2 Preparation of $NH_4V_4O_{10}$ Cathode

1.170 g NH_4VO_3 was dissolved in 70 ml deionized water at 70°C, and then 1.891 g $H_2C_2O_4·2H_2O$ powder was added to the NH_4VO_3 solution with magnetic stirring. After complete dissolution, the solution was transferred to a 100 ml autoclave and heated at 140°C for 12 h. After the sample was cooled to room temperature, the product was collected, washed repeatedly with deionized water, and then dried at 60°C for 12 h to finally obtain $NH_4V_4O_{10}$ powder.[1]

The $NH_4V_4O_{10}$ powder was mixed with acetylene black and PVDF in NMP in a weight ratio of 7:2:1, which was then coated onto a piece of stainless steel. The coated stainless steel was dried at 80°C for 8 h, and the $NH_4V_4O_{10}$ cathode was obtained.

1.3 Material Characterization

The X-ray diffraction (XRD) pattern of the power was obtained by Ultima IV using Cu K_α-radiation (λ = 0.1541 nm) with a scan speed of 10°/min. Fourier infrared spectra (FTIR) were measured in the range of 4000 to 400 cm^{-1} using a PerkinElmer Spectrum 3 spectrometer. The microscopic morphology of the sample surface and cross-section was characterized on a Zeiss Sigma 300 (Germany) field emission electron microscopy (SEM). X-

ray photoelectron spectroscopy (XPS) data were recorded on Thermo Scientific K-Alpha (America) to analyze the binding energy and compositional composition of the samples. Additionally, the stress-strain curves and electrolyte wetting of the separator were demonstrated by a universal tensile machine (Model: CMT6014, Xinsansi) and a contact angle tester (HARKE-SPCA-1).

1.4 Battery assembly and electrochemical measurements

The battery assembly and the electrochemical measurements were all conducted at 25 ± 1°C. The Zn||Zn symmetrical cell consists of a Zn plate with a diameter of 12 mm as the electrode and different types of separators to investigate the cycling performance of the cell. The Zn||Cu half-cells were prepared according to the symmetrical methods, with the exception that one side of the Zn plate is substituted by Cu foil. The electrolyte used for the above symmetrical cell and half-cells is 2 M $ZnSO_4$. The Zn||NVO full cell was assembled with Zn anode and NVO cathode, with 3 M $ZnSO_4$ as the electrolyte. All tested CR2032-type coin cells were assembled in the air.

The cycling performance and galvanostatic charge/ discharge (GCD) data of the cells were recorded by Batter Testing System (Neware, China). The various separator assemblies of Zn||Zn symmetric cells were tested at different current densities. Meanwhile, galvanostatic charge/discharge of Zn||NVO full cell was carried out in the range of 0.4~1.4 V.

The cyclic voltammetry (CV), electrochemical impedance spectroscopy (EIS), Tafel plots, chronoamperometry (CA) and ionic transfer number were recorded via the Admiral electrochemical system. The CV measurements of the Zn||NVO full cell were tested at a sweep rate of 1 mV/s over a voltage window test range of 0.4 to 1.4 V. EIS measurements were conducted with a frequency ranging from 10^{-2} to 10^{4} Hz. Tafel test was performed between -0.3 V and 0.3 V under 1 mV/s. CA measurements were conducted in symmetric cells under -150 mV.

1.5 Calculating the characteristics of separators

Calculation of porosity. The porosity of the separator was calculated by the following method. The separator was immersed in n-butanol solution for 2 h, and then the excess n-butyl alcohol on the surface was absorbed with filter paper. W_a and W_b are the mass of the separator before and after immersion. The porosity was calculated according to equation (1)[2]:

$$P = \frac{W_b/\rho_b}{W_a/\rho_a + W_b/\rho_b} \times 100\% \quad (1)$$

where ρ_a and ρ_b represent the density of separator and n-butyl alcohol, respectively.

Calculation of electrolyte uptake. The electrolyte uptake was obtained via immersing the separator in the electrolyte for 2 h and calculated by equation (2)[3]:

$$U = \frac{W_1 - W_0}{W_0} \times 100\% \quad (2)$$

where W_0 and W_1 are the mass of the separator before and after immersion, respectively.

Calculation of ionic conductivity. The SS||SS cell was prepared by replacing the Zn plate with a stainless steel (SS) plate in the standard Zn||Zn symmetric cell assembly, using different separators to eliminate Faradaic interference. The ionic conductivity was measured by EIS test at 10^4-10^{-2} Hz with an AC perturbation voltage of 5 mV and calculated using the following equation (3)[4]:

$$\sigma = \frac{L}{AR_0} \quad (3)$$

where L and A are the thickness and area of the SS, respectively, and R_0 represents the resistance according to EIS measurement.

Calculation of ionic transference number. Zn^{2+} ionic transference numbers were assessed through EIS and CA on Zn||Zn symmetrical cell, and were calculated by the following equation (4)[5]:

$$\tau_{Zn^{2+}} = \frac{I_s}{I_0} \times \frac{V - I_0 R_0}{V - I_s R_s} \quad (4)$$

where V is applied polarization voltage (10 mV), I_0 and Is are the initial and steady-state current values during polarization, and R_0 and R_s are the resistance values before and after polarization at constant potential, respectively.

The battery assembly and the data measurements for the above calculations were conducted at 25 ± 1°C.

1.6 DFT calculations

The binding energy of Zn^{2+} with different targets (H_2O, CF separator and VF separator) was defined by equation (5):

$$E_{binding\ energy} = E_{Zn^{2+}} + E_{targets} - E_{Zn^{2+}/targets} \quad (5)$$

where $E_{Zn^{2+}}$ and $E_{targets}$ were the total energy of Zn^{2+} and targets directly obtained from the density functional theory (DFT) calculations using Materials Studio (MS), respectively, and $E_{Zn^{2+}/targets}$ was the total energy of optimized Zn^{2+}-targets.

Therefore, the energies of Zn^{2+}, H_2O, CF, VF, Zn^{2+}-H_2O, Zn^{2+}-CF, Zn^{2+}-VF (referred to as calculation objects) should be obtained in three steps. Firstly, the "Energy" program in Forcite was employed to endow the charges and force fields of calculation objects using the

COMPASS II force field. Secondly, the "Anneal" program was utilized to perform the annealing treatment of calculation objects. The annealing process consisted of 100 cycles, with an annealing temperature of 300.0 K and a medium cycle temperature of 500.0 K. Each cycle included 5 heating ramp steps, and each ramp consisted of 100 dynamic steps. The COMPASS II force field was used. Finally, the "Geometry Optimization" in the Dmol^3 module was employed to perform geometry optimization. Finally, the Generalized Gradient Approximation (GGA) with the Perdew-Burke-Ernzerhof (PBE) exchange-correlation function was used to fully relax the calculation objects. The calculations were conducted to obtain their energies without spin restriction and without using symmetry information. The convergence tolerances were set as follows: energy tolerance of 2×10^{-5} Ha, maximum force of 0.004 Ha/Å, maximum displacement of 0.005 Å, maximum number of iterations of 1000, and maximum step size of 0.3 Å. In the Self-Consistent Field (SCF) procedure, the SCF tolerance was 1.0×10^{-5}, the maximum number of cycles was 99999, and the multipole expansion type was hexadecapole. For density mixing, the charge was set to 0.2, and the rotation was 0.5. The Direct Inversion in the Iterative Subspace (DIIS) method was used with a size of 6. In the orbital occupancy, the Fermi smearing method was applied to accelerate convergence, with a smearing value of 0.005 Ha.

2. Physical properties of separators

Electrolyte affinity. The electrolyte affinity of GF, FP, CF, BF and VF was revealed by the dynamic contact angle measurement (Figure S1). GF and VF separators take only 0.04 s to absorb the electrolyte drops, while CF, FP and BF take 0.11 s, 0.30 s and 0.54 s, respectively, indicating that VF has excellent electrolyte affinity as well as GF.

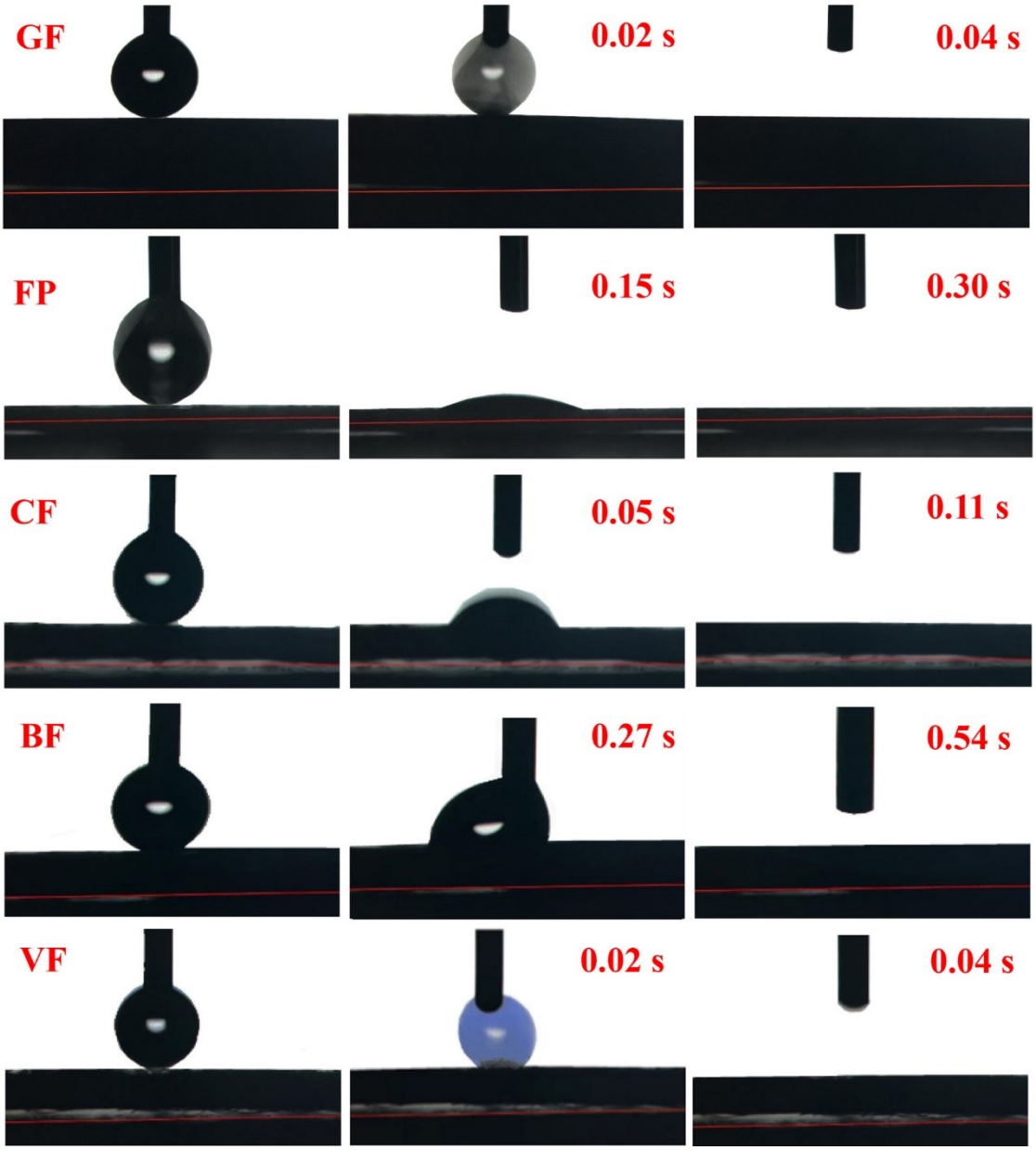

Figure S1. Dynamic contact angles of GF, FP, CF, BF and VF separators with electrolyte.

Electrolyte uptake and porosity. Figure S2 represents the electrolyte uptake and porosity of GF, FP, CF, BF and VF separators. It can be found that all separators have a high porosity of larger than 50%. The electrolyte uptake of GF, CF, BF and VF separators is all higher than 800% because of their hydrophilic, loose and porous characteristics. FP separator possesses relatively low electrolyte uptake of only about 200% because the fibers in FP separator are glued with each other by the binding agents.

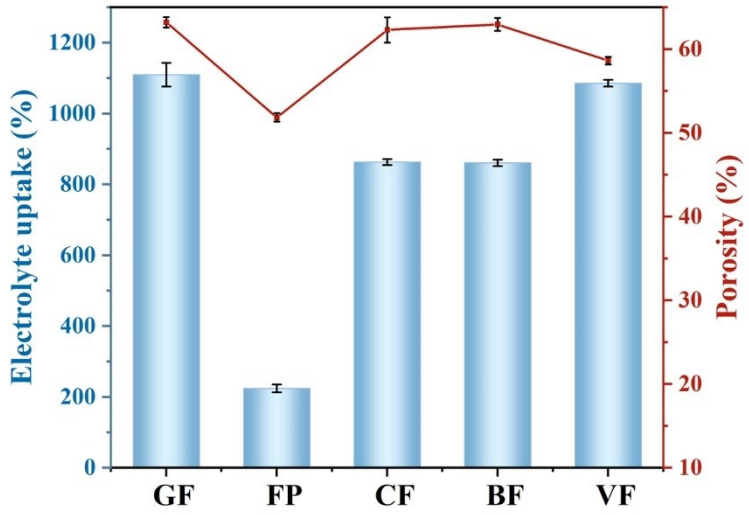

Figure S2. Electrolyte uptake and porosity of GF, FP, CF, BF and VF separators.

Comment for Figure S3: The GF separator consists of randomly stacked rigid GF fibers with weak inter-fiber interactions. As a result, both GF with and without electrolyte impregnation exhibit brittle fracture with minimal strain (Figure S3). In contrast, the FP separator, which contains fibers bonded by a binding agent (e.g., polyvinyl alcohol), demonstrates high tensile strength in its dry state. However, upon electrolyte impregnation, its tensile strength significantly deteriorates due to the loss of adhesion of the binding agent in the wet state and the absence of fiber entanglement. Conversely, the repeated spunlace processing of CF, BF, and VF facilitates fiber entanglement (Figure S4), thereby substantially enhancing their mechanical properties, both with and without electrolyte impregnation (Figure S3a-c). Furthermore, CF, BF, and VF are composed of polymer fibers, whose inherent viscoelasticity and flexibility mitigate brittle fracture (Figure S3a, b). As shown in Figure S3c, the tensile strengths of electrolyte-impregnated CF, BF, and VF exceed those of GF and FP by more than an order of magnitude. This enhanced mechanical robustness plays a crucial role in impeding Zn dendrite penetration and preventing short circuits in cells.

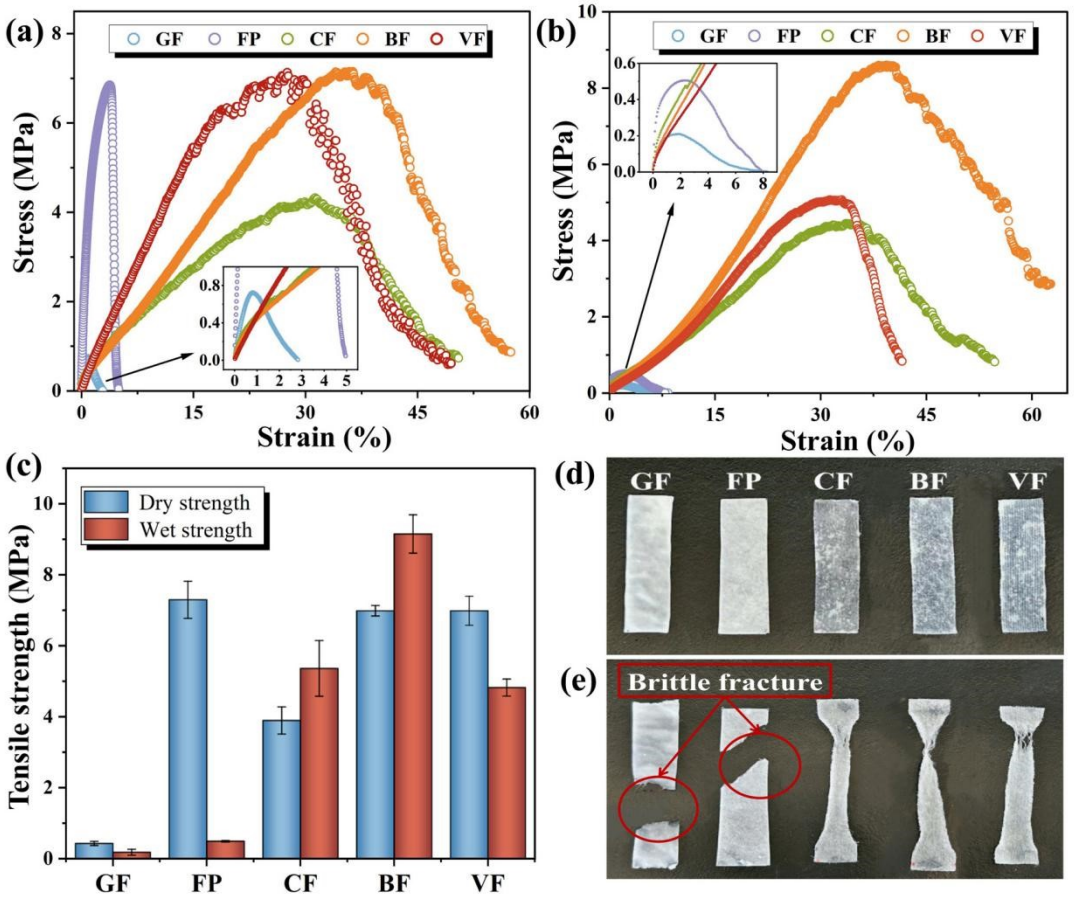

Figure S3. Mechanical properties of GF, FP, CF, BF and VF separators. Stress-strain curves of separators (a) without and (b) with electrolyte impregnation. (c) Tensile strength of separators; Photos of separators (d) before and (e) after tensile strength test.

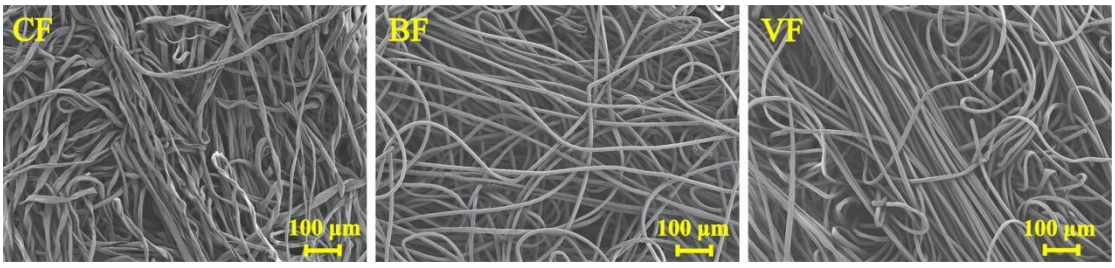

Figure S4. SEM image of entanglement of fibers in CF, BF and VF separators.

3. Cycling stability

The thickness values of one-layer GF, FP, CF, BF and VF separators are shown in Figure S5, which are 0.675 mm, 0.197 mm, 0.260 mm, 0.267 mm and 0.265 mm, respectively.

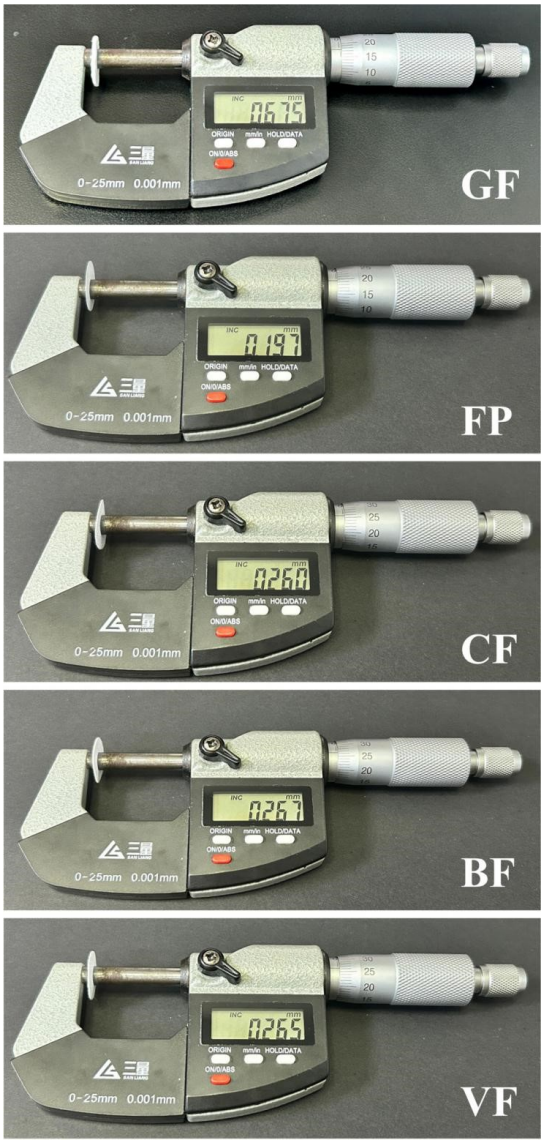

Figure S5. Thickness values of single-layer GF, FP, CF, BF and VF separators.

Comment for Figure S6: As shown in Figure S6, we assembled Zn||Zn symmetric cells to test the cycle life of five different separators under the test conditions of 2 mA cm^{-2} with a capacity of 4 mAh cm^{-2}. The cycle life of the cells with GF, FP, CF, BF and VF separators was 30 h, 3 h, 5 h, 1 h and 1 h, respectively. At the same time, we also explored the cycle life of the Zn||Zn symmetric cells with these five separators under the test conditions of 4 mA cm^{-2} with a capacity of 4 mAh cm^{-2} (Figure S7). The results showed that the cycle life of GF separator reached 37 h due to its large thickness, while the cycle life of FP, CF, BF and VF separators was 6 h, 9 h, 1 h and 1 h, respectively. The poor cycling performance of CF, BF

and VF separators at higher current density is attributed to the loose structure of fibers within the separators and the large pores between fibers.

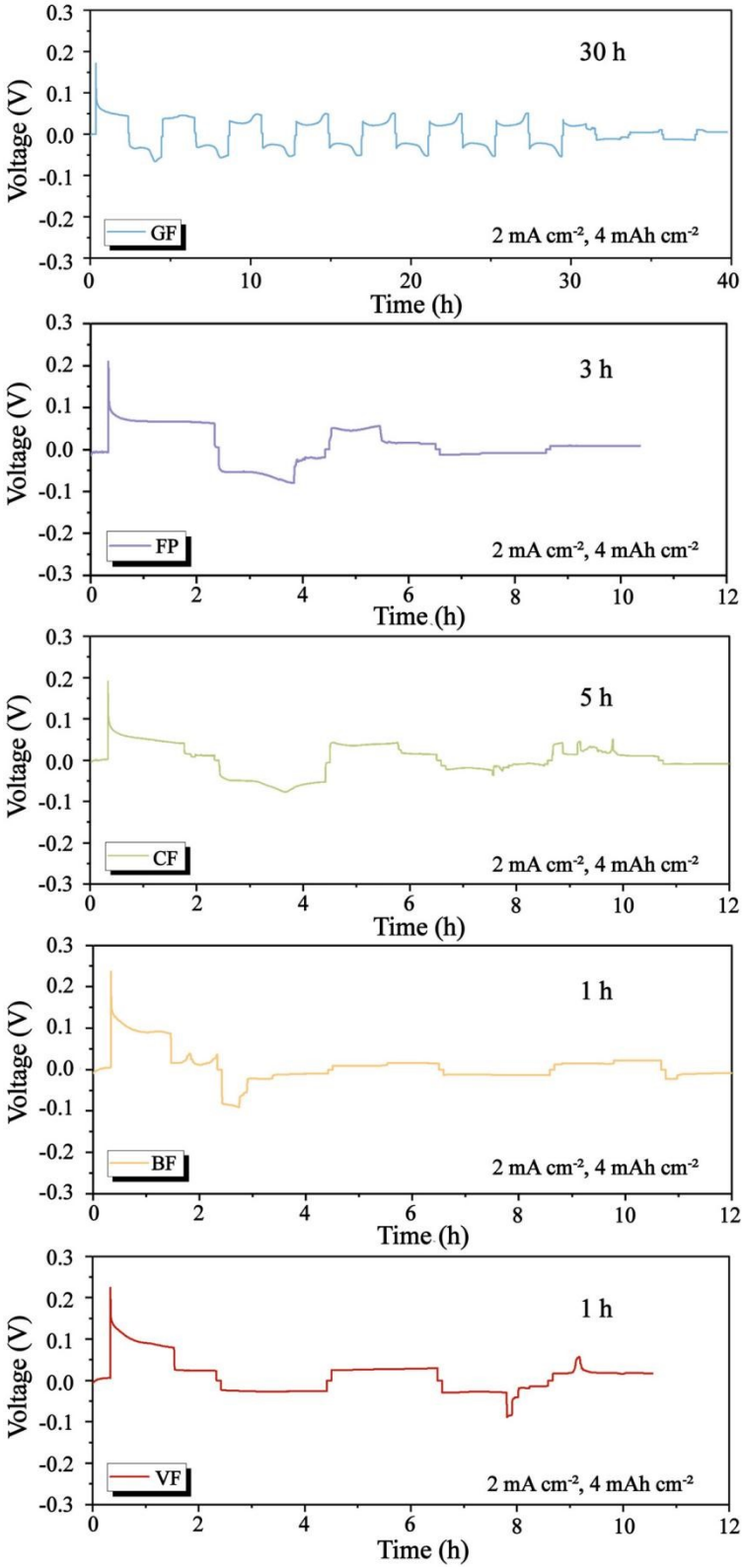

Figure S6. Cycling performance of symmetric cells with GF, FP, CF, BF and VF separators at 2 mA cm^{-2} with a capacity of 4 mAh cm^{-2}.

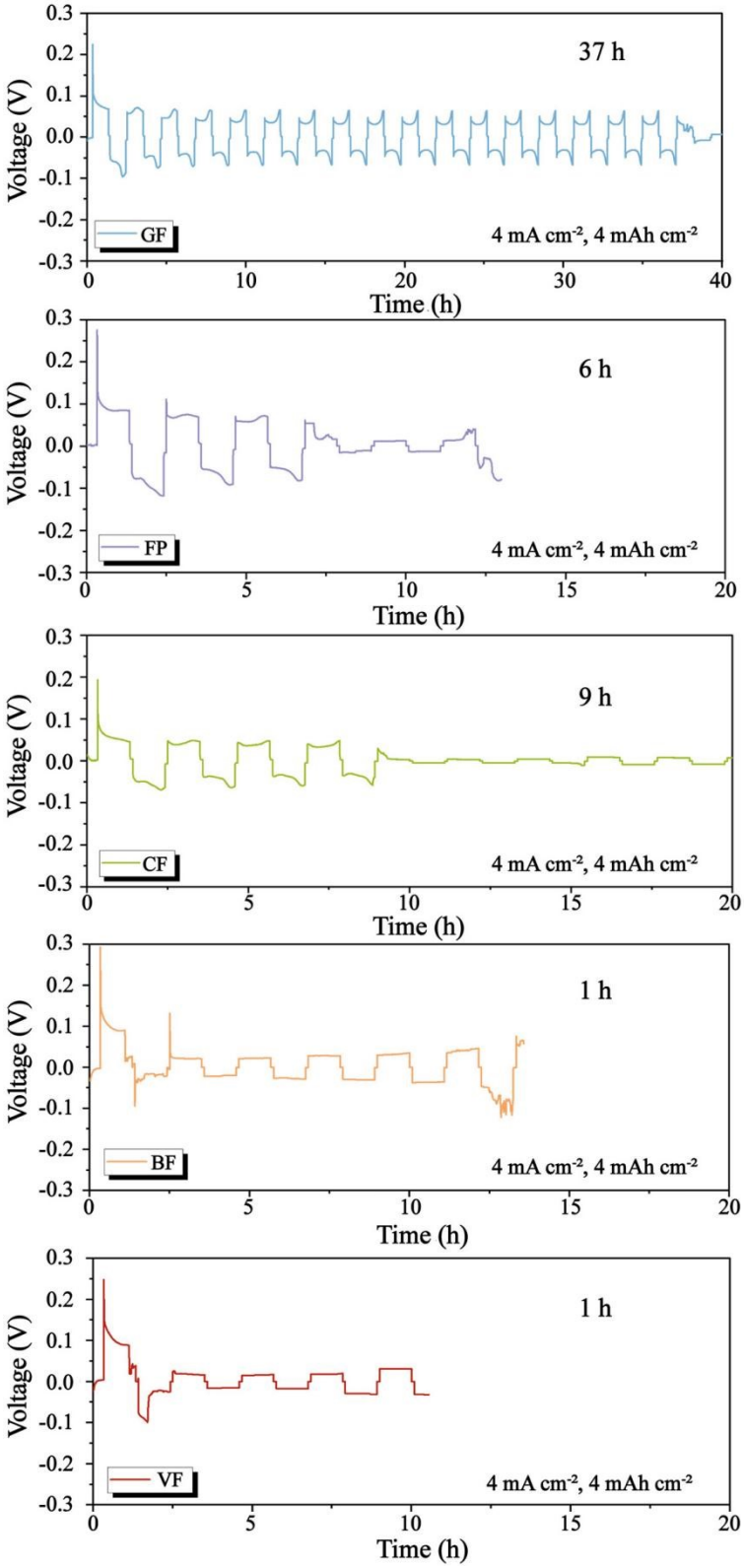

Figure S7. Cycling performance of symmetric cells with GF, FP, CF, BF and VF separators at 4 mA cm^{-2} with a capacity of 4 mAh cm^{-2}.

Therefore, two layers CF, BF and CF are stacked together (Figure S8, named 2CF, 2BF and 2VF) to provide the separator with greater thickness and more uniform pores, much like GF separator. Symmetric cells with 2CF, 2BF and 2VF are also assembled for cycling tests. Surprisingly, cells with a 2VF separator cycled for about 1180 h and 620 h at 2 mA cm^{-2} with a capacity of 4 mAh cm^{-2} and 4 mA cm^{-2} with a capacity of 4 mAh cm^{-2}, respectively (Figure S9 and S10), while cells equipped with 2CF and 2BF separators short-circuit after a short cycling. These indicate that VF separator can also endow cells with good cycling stability under harsher conditions.

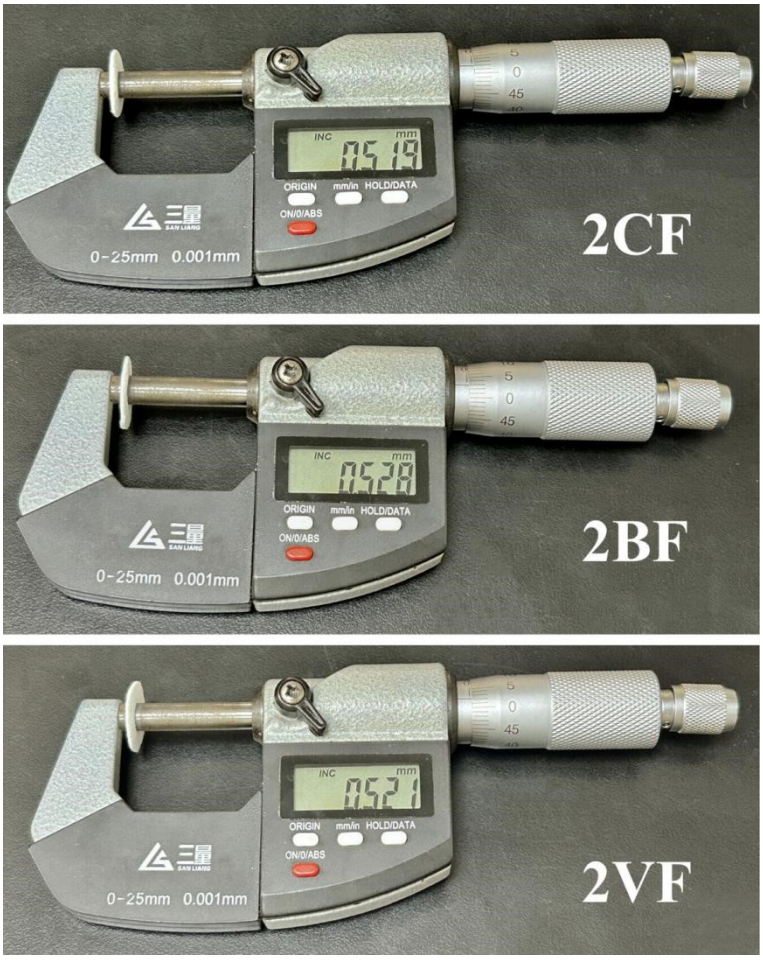

Figure S8. Thickness values of 2CF, 2BF and 2VF separators.

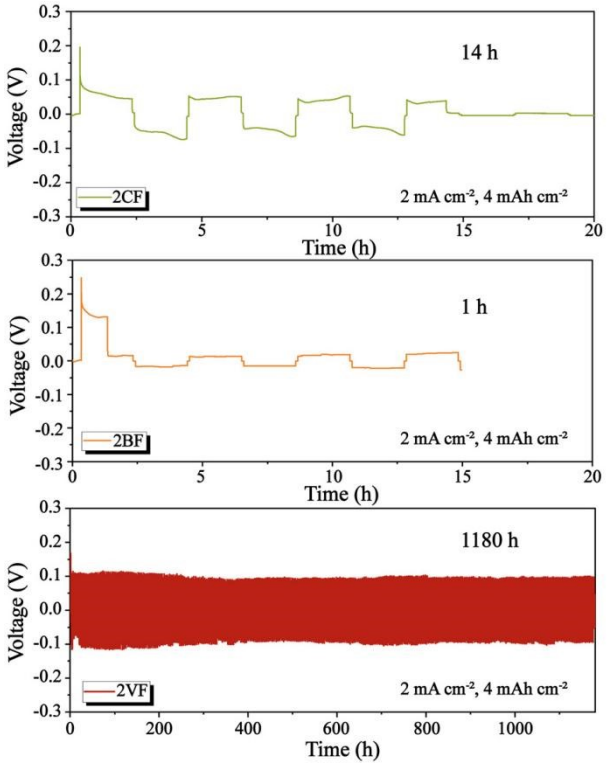

Figure S9. Cycling performance of symmetric cells with 2CF, 2BF and 2VF separators at 2 mA cm^{-2} with a capacity of 4 mAh cm^{-2}.

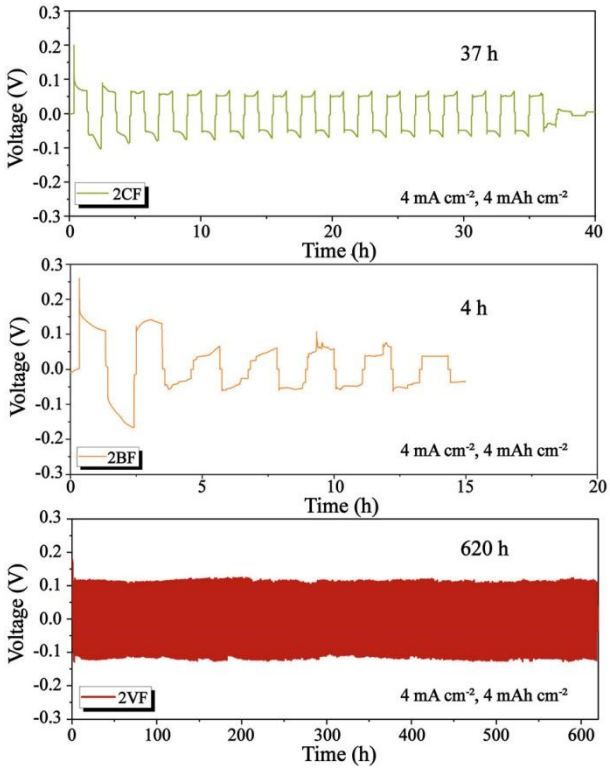

Figure S10. Cycling performance of symmetric cells with 2CF, 2VF and 2BF separators at 4 mA cm^{-2} with a capacity of 4 mAh cm^{-2}.

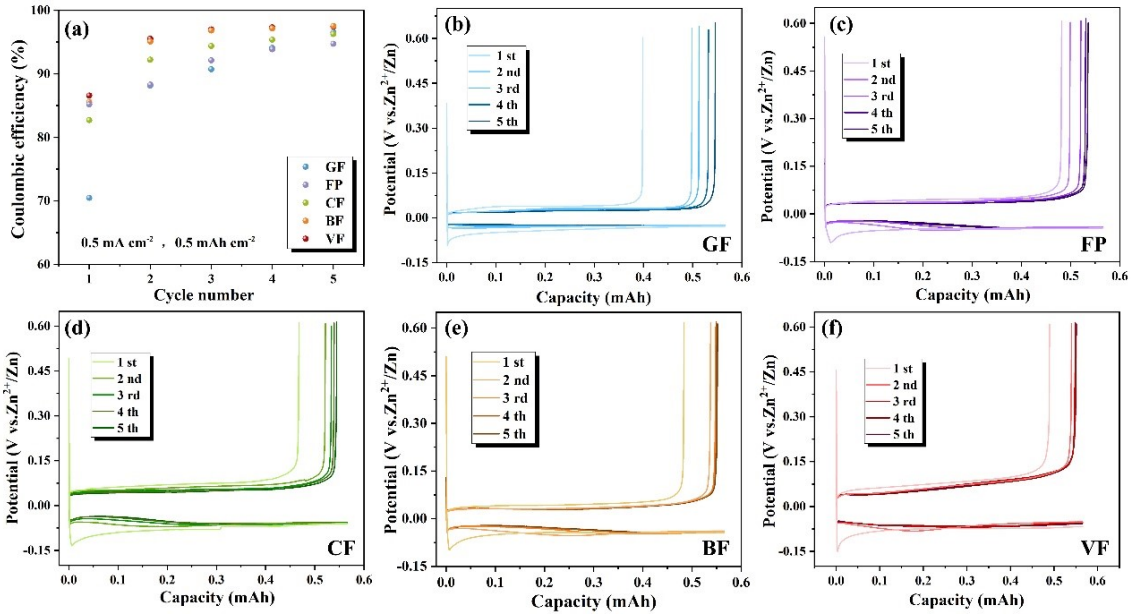

Figure S11. Coulomb efficiency of GF, FP, CF, BF and VF separators in the five cycles at 0.5 mA cm^{-2} with a capacity of 0.5 mAh cm^{-2}.

4. Zn deposition and HER

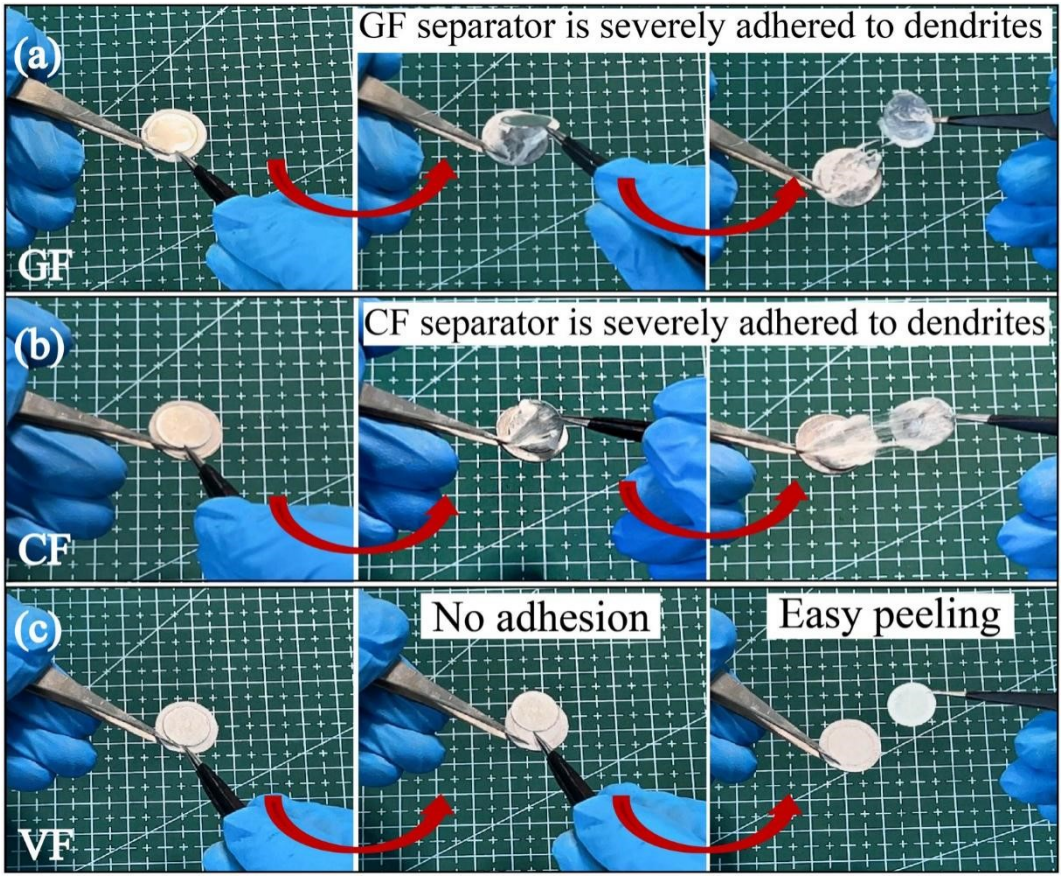

Figure S12. Cell disassembly diagram of GF, CF and VF separators equipped cells.

Table S1. Performance comparison of Zn symmetric cells with VF separator and the reported separators

Material	Preparation method	Price /¥·m^{-2}	Current density	Life span/h	Ref.
GF	Janus separator (via growing vertical graphene carpet on one side of GF)	5500	1 mA cm^{-2}, 1 mAh cm^{-2}	250	6
GF	NC/GF (in situ grow NC over GF via plasma-enhanced chemical vapor deposition)	3200	1 mA cm^{-2}, 1 mAh cm^{-2}	1100	7
GF	MXene-GF (spray-printing MXene nanosheets over one side of GF)	5721	1 mA cm^{-2}, 1 mAh cm^{-2}	1180	8
GF	GF@SM (melamine and cyanuric acid were added into DMSO, and then dripped on the GF)	4070	1 mA cm^{-2}, 1 mAh cm^{-2}	2000	9
GF	GF-PNAI (in situ polymerization of aniline monomers on one side of the GF)	3890	1 mA cm^{-2}, 1 mAh cm^{-2}	3000	10
GF	MOF-808 (the use of Zr-MOFs to modify GF)	4375	0.1 mA cm^{-2}	350	11
Filter membrane	/	140	1 mA cm^{-2}, 1 mAh cm^{-2}	2600	12
WP	insert between Zn anode and separator	20.15	1 mA cm^{-2}, 1 mAh cm^{-2}	2400	13
CNF	Zr^{4+}-hydrolysate-coated CNF	60	1 mA cm^{-2}, 1 mAh cm^{-2}	1600	14
CNF	F-CNF (modified CNF with zincophilic site-rich C/Cu nanocomposite decoration layer)	180	1 mA cm^{-2}, 0.5 mAh cm^{-2}	2000	15
CM	CCM (the carbonylation modification cellulose membranes)	20	1 mA cm^{-2}, 1 mAh cm^{-2}	2800	16
Cellulose	ZC (prepared from the ZrO_2 particles and polymethyl cellulose in solution casting method)	9.14	0.5 mA cm^{-2}, 0.25 mAh cm^{-2}	2000	17
Cellulose	CG (synthesis of cellulose/graphene oxide via a solution casting method)	37	0.5 mA cm^{-2}, 0.25 mAh cm^{-2}	1750	2
Cotton	CT (commercially available cotton towels)	5	1 mA cm^{-2}, 0.5 mAh cm^{-2}	1200	18
Cotton	CF separator (pretreated with NaOH, H_2O_2, and vacuum filtrated)	7.32	1 mA cm^{-2}, 1 mAh cm^{-2}	2000	5
GF	/	3100	1 mA cm^{-2}, 1 mAh cm^{-2}	52	This work
FP	/	18.95		22	
CF	Commercial spunlace nonwoven fabric	6.25		7	
BF		2.21		2	
VF		3.21		4600	

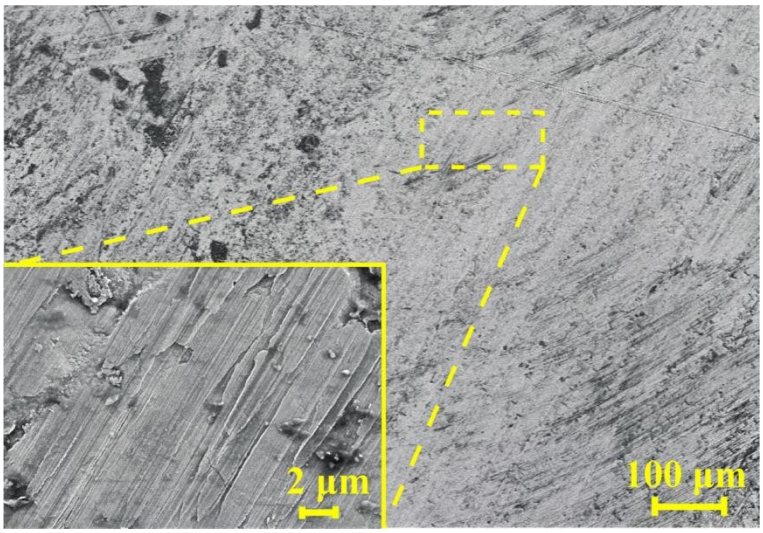

Figure S13. SEM image of bare Zn foil.

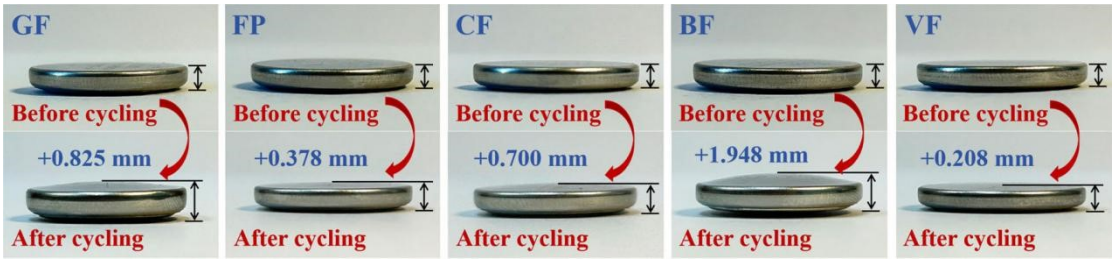

Figure S14. Cell bulge diagrams for GF, FP, CF, BF, and VF separators.

5. Chemical structure of CF and VF

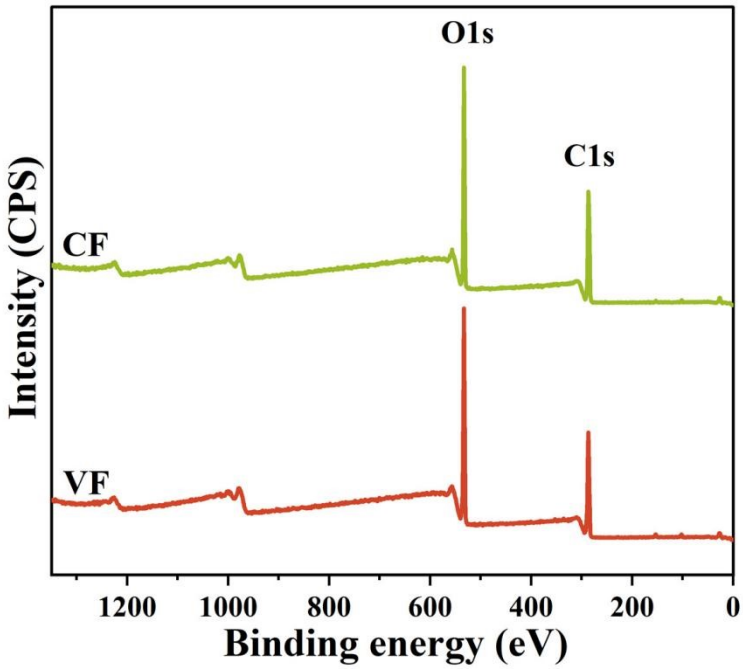

Figure S15. XPS spectra of CF and VF separators.

Table S2. Surface element and functional group distribution of CF and VF separators by XPS

Samples	Element concentration/%			The ratio of functional groups(C1s)/%			
	C	O	S	C1	C2	C3	C4
CF	62.95	36.59	0.46	32.59	39.46	27.95	/
VF	58.88	40.75	0.36	22.94	37.26	24.20	15.60

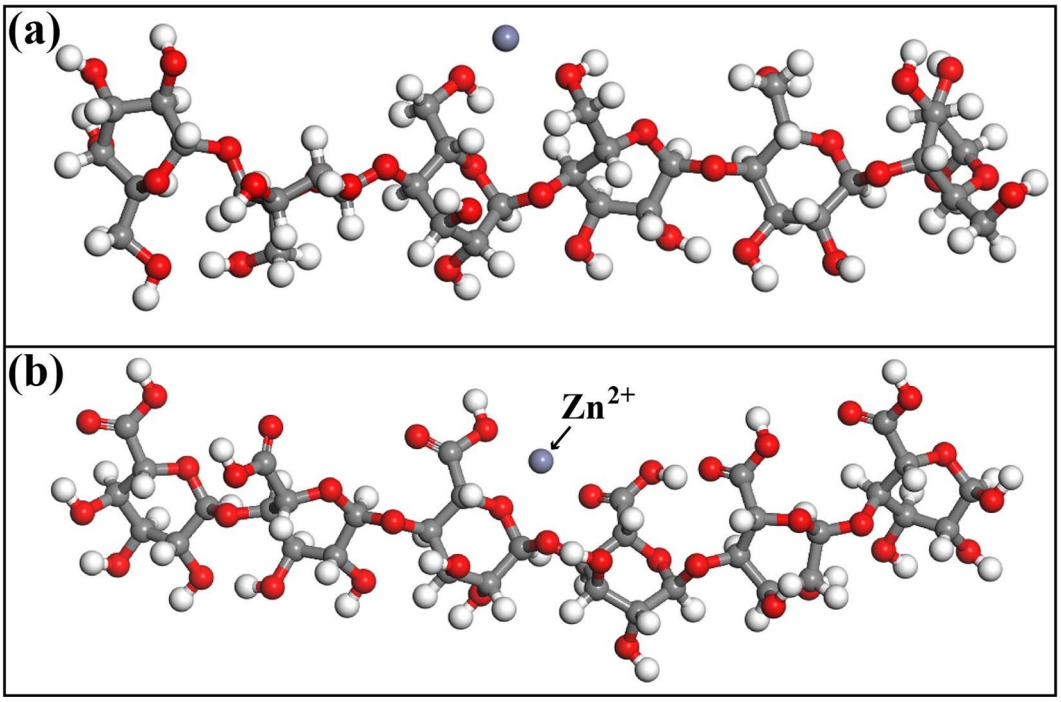

Figure S16. Schematic diagram of fragments of cellulose molecule (a) and viscose molecule (b)

Table S3. The binding energies of Zn^{2+} to CF separator from DFT calculations.

Zn^{2+}-CF (Ha)	CF (Ha)	Zn^{2+} (Ha)	Eint (Ha)	Eint (kcal/mol)
-5516.51	-3737.92	-1778.16	-0.42895	-269.17

Table S4. The binding energies of Zn^{2+} to VF separator from DFT calculations.

Zn^{2+}-VF (Ha)	VF (Ha)	Zn^{2+} (Ha)	Eint (Ha)	Eint (kcal/mol)
-5960.81	-4182.06	-1778.16	-0.59439	-372.98

Table S5. The binding energies of Zn^{2+} to H_2O from DFT calculations.

Zn^{2+}-H_2O (Ha)	H_2O (Ha)	Zn^{2+} (Ha)	Eint (Ha)	Eint (kcal/mol)
-1854.66	-76.3518	-1778.16	-0.14953	-93.83

6. TEMPO oxidized-CF separator

1 g of CF, 0.016 g TEMPO (>98%, Aladin, China), and 0.16 g NaBr (AR, Sinophar, China) were added into 100 mL of deionized water and stirred thoroughly. NaClO (AR,

Sinophar) with a molar mass concentration of 5 mmol/g was added into the above solution, and then 0.5 mol/L NaOH (AR, Sinophar, China) aqueous solution was continuously dropped during the reaction process to maintain the pH value to be 10.0 ± 0.2. After reacting at 30°C for 4 h, 10 mL anhydrous ethanol was added to terminate the reaction and the pH was adjusted to be neutral with 0.5 mol/L HCl (AR, Sinophar, China). Finally, the TEMPO-oxidized CF was washed with water and dried at 60°C.[19]

Figure S17 shows FTIR spectra of CF, oxidized-CF and oxidized-CF immersed with electrolyte. The introduction of carboxyl groups and their coordination effect with Zn^{2+} has not been found in FTIR spectra. This is because the oxidation of CF only happens on the surface of cotton fibers, and therefore carboxyl groups are only introduced onto the cellulose molecules on the surface of cotton fiber. For cotton fibers with a diameter of approximately 15 μm, the proportion of surface cellulose molecules relative to the entire cotton fiber is very low. Consequently, the amount of carboxyl groups introduced constitutes an extremely low proportion of the whole cotton fiber and is undetectable by FTIR.

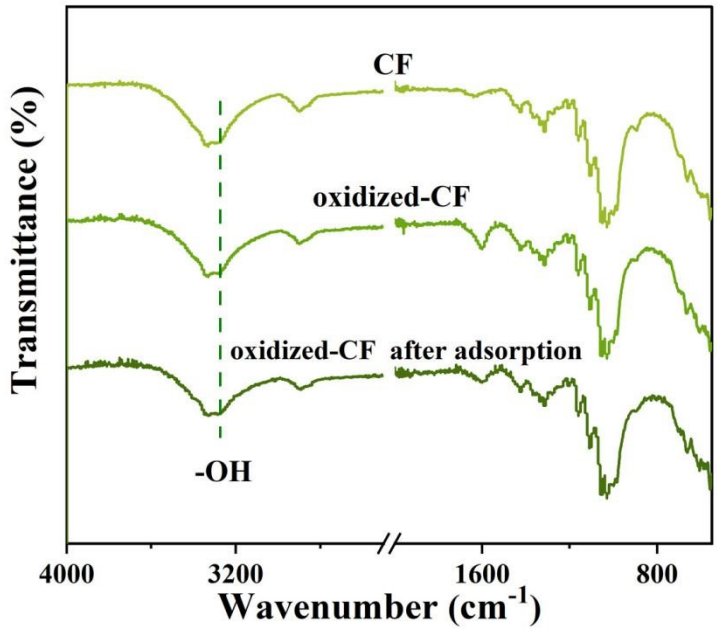

Figure S17. FTIR spectra of CF, oxidized-CF and oxidized-CF immersed with electrolyte.

XPS is a surface analysis technique with a testing depth of about 10 nm, making it a commonly used method for characterizing the chemical structure of materials' surfaces. Figure S18 and Table S6 show that the oxygen content increases from 31.08% to 36.88% after TEMPO oxidation. This is mainly owing to the introduction of carboxyl groups onto the CF surface by oxidation of primary hydroxyl groups of cellulose into carboxyl groups. Figure S19 shows the high-resolution C1s spectra of CF and oxidized CF. For oxidized CF, the additional peak at 288.8 eV is attributed to carboxyl groups, demonstrating convincingly the

oxidation of primary hydroxyl groups of cellulose into carboxyl groups. In summary, FTIR does not find the carboxyl groups, while XPS does, indicating that the TEMPO oxidation of cotton fibers is a surface-limited oxidation process, which will not significantly alter the microstructure of the cotton fibers.

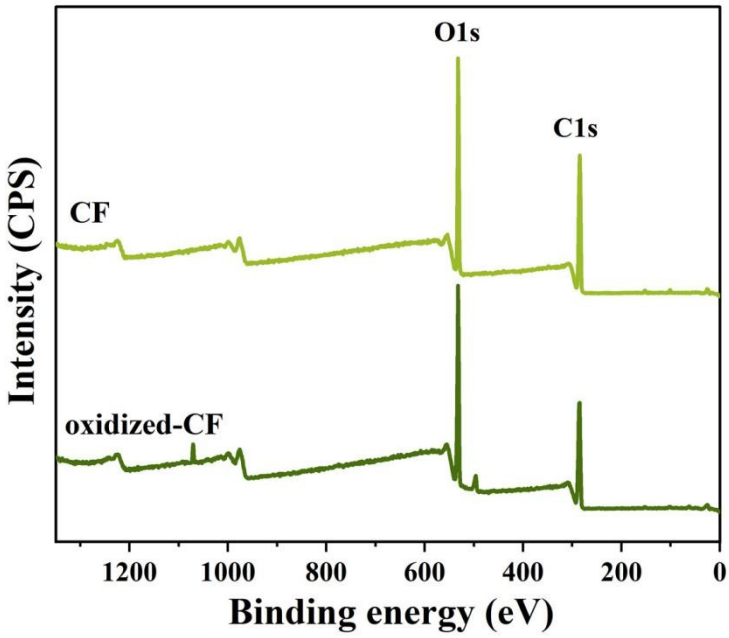

Figure S18. XPS spectra of CF and oxidized-CF.

Table S6. Surface element and functional group distribution of CF and oxidized-CF by XPS

Samples	Element concentration/%			The ratio of functional groups (C1s)/%			
	C	O	S	C1	C2	C3	C4
CF	68.57	31.08	0.35	39.16	41.85	18.99	/
oxidized-CF	62.85	36.88	0.27	20.59	41.56	26.80	11.05

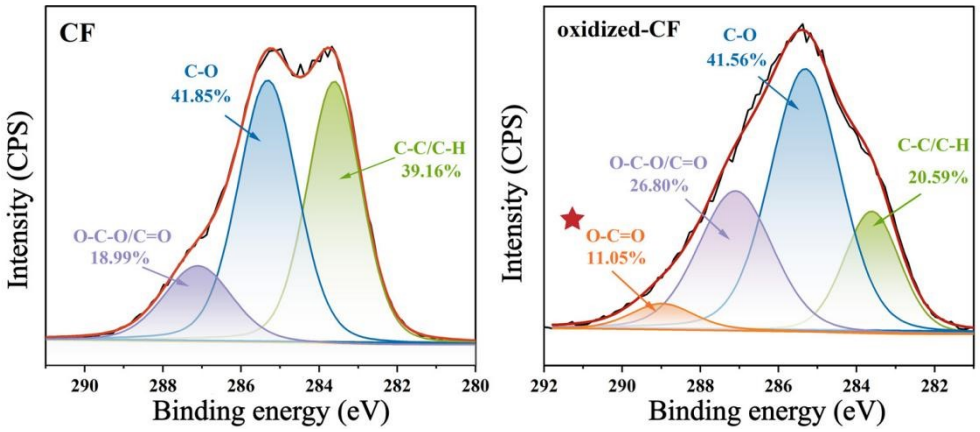

Figure S19. High-resolution C1s spectra of CF and oxidized-CF.

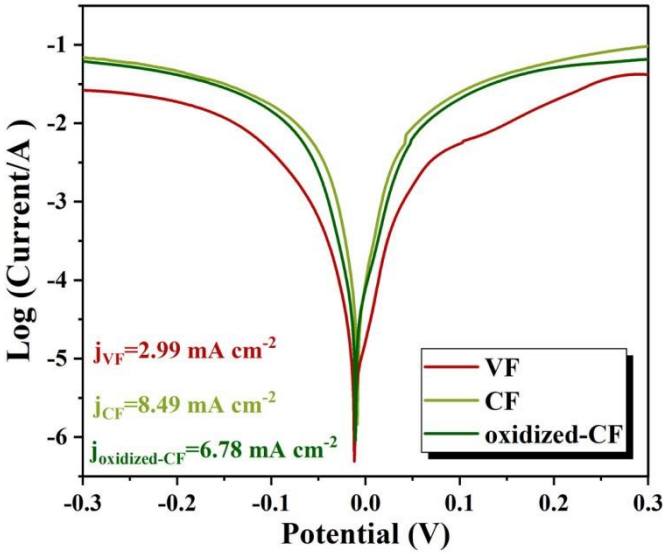

Figure S20. Tafel plots of the cells with CF, oxidized-CF and VF separators.

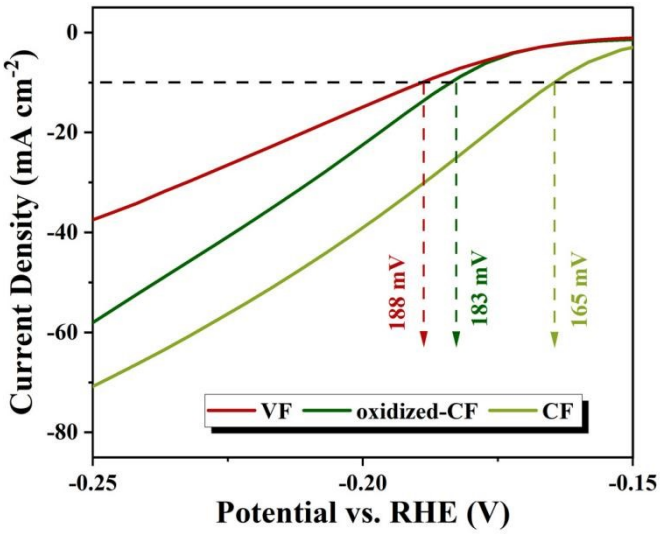

Figure S21. The hydrogen evolution potential of the cells with CF, oxidized-CF and VF separators.

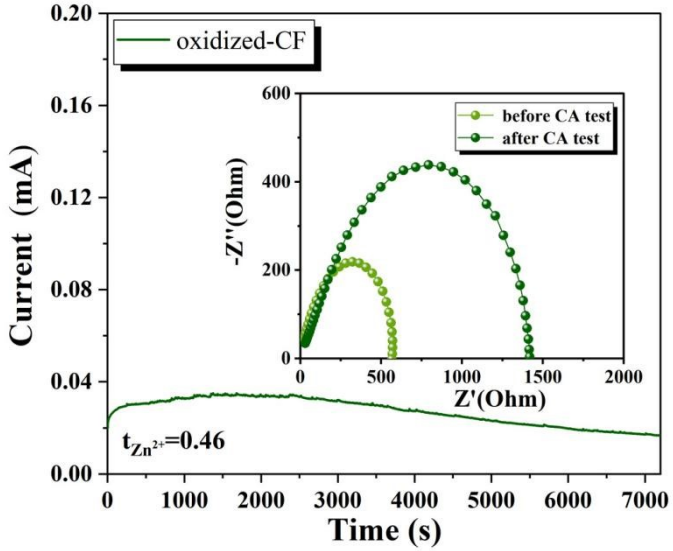

Figure S22. Zn^{2+} transference number of oxidized-CF separator.

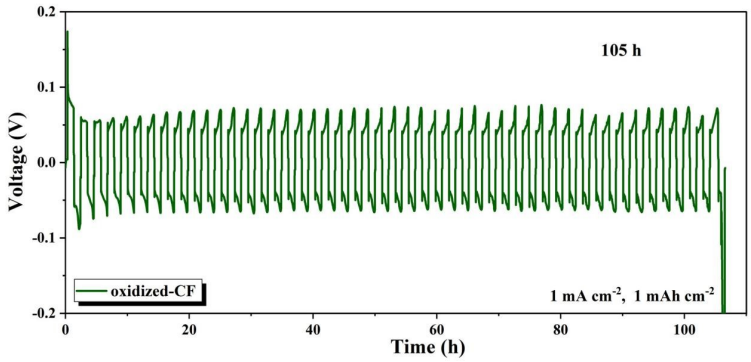

Figure S23. Cycle life of Zn|oxidized-CF|Zn symmetric cell.

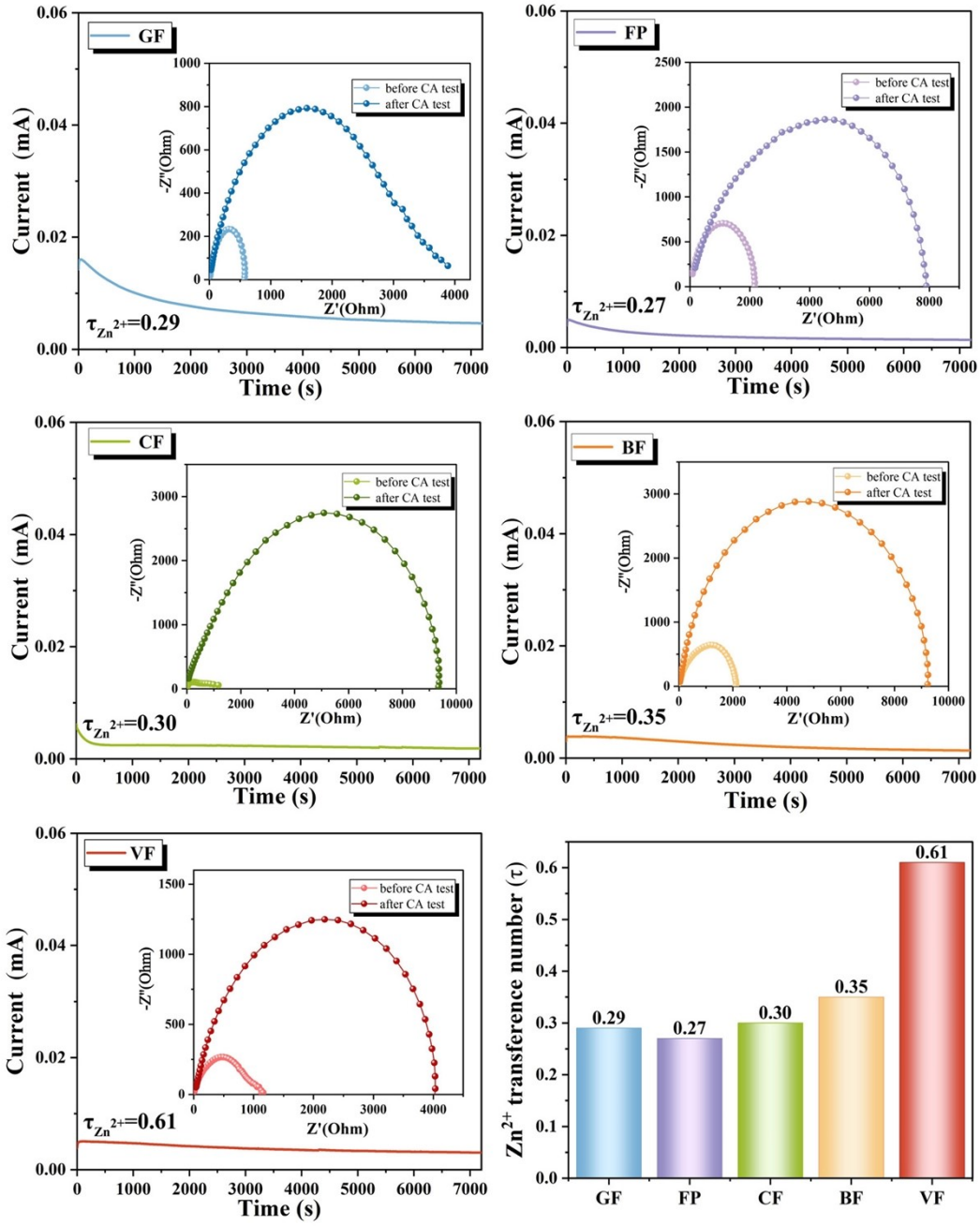

Figure S24. Zn^{2+} transference number of GF, FP, CF, BF and VF separators.

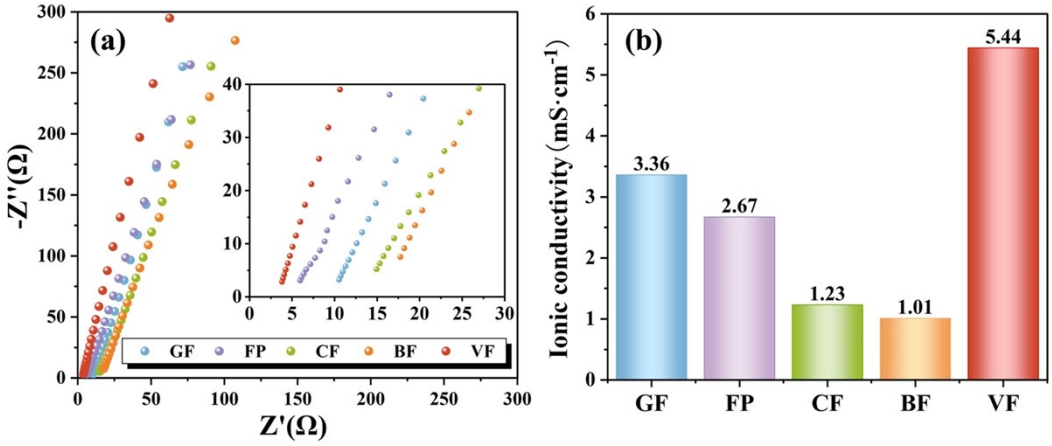

Figure S25. EIS and ionic conductivity of GF, FP, CF, BF and VF separators.

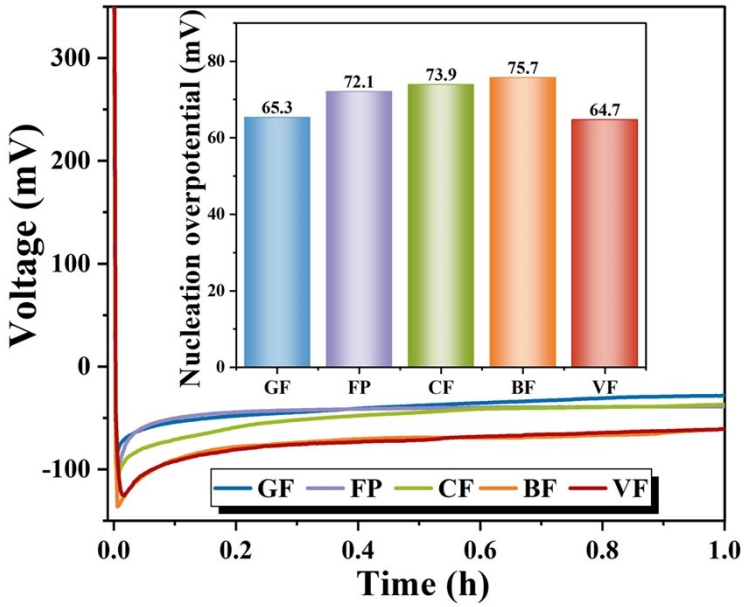

Figure S26. Nucleation overpotential of GF, FP, CF, BF and VF separators

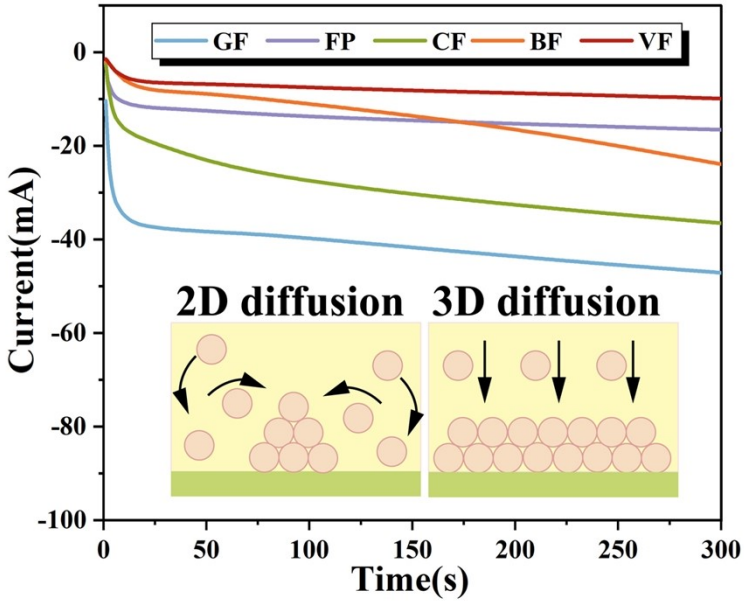

Figure S27. CA test of the cell with GF, FP, CF, BF and VF separators.

Table S7. Electrolyte uptake and porosity of GF, FP, CF, BF and VF separators.

Samples	GF	FP	CF	BF	VF
Price[a]//¥·m^{-2}	3100	19	6	2	3
Tensile property[b]/MPa	0.18±0.08	0.49±0.02	5.36±0.78	9.15±0.54	4.82±0.24
Porosity/%	63.20±0.62	51.84±0.51	62.28±1.5	62.95±0.77	58.62±0.44
Electrolyte uptake/%	1109.41±33.37	223.99±10.95	862.93±8.21	860.51±9.38	1085.42±9.50
Electrolyte affinity[c]/s	0.04	0.30	0.11	0.54	0.04
Ionic conductivity/mS cm^{-1}	3.36	2.67	1.23	1.01	5.44
Ion transference number	0.29	0.27	0.30	0.35	0.61
Life span/h	52	22	7	2	4600
Discharge capacity[d]/mAh g^{-1}	18.25	8.03	53.45	66.15	92.93

[a] The prices are all sourced from inquiries on the official Alibaba website.

[b] The listed items are the tensile property of the separator after absorbing the electrolyte.

[c] The electrolyte affinity is characterized by the dynamic contact angle of the separator material, with the electrolyte penetration and absorption rate serving as the evaluation metric.

[d] The discharge specific capacity at the 1000th cycle.

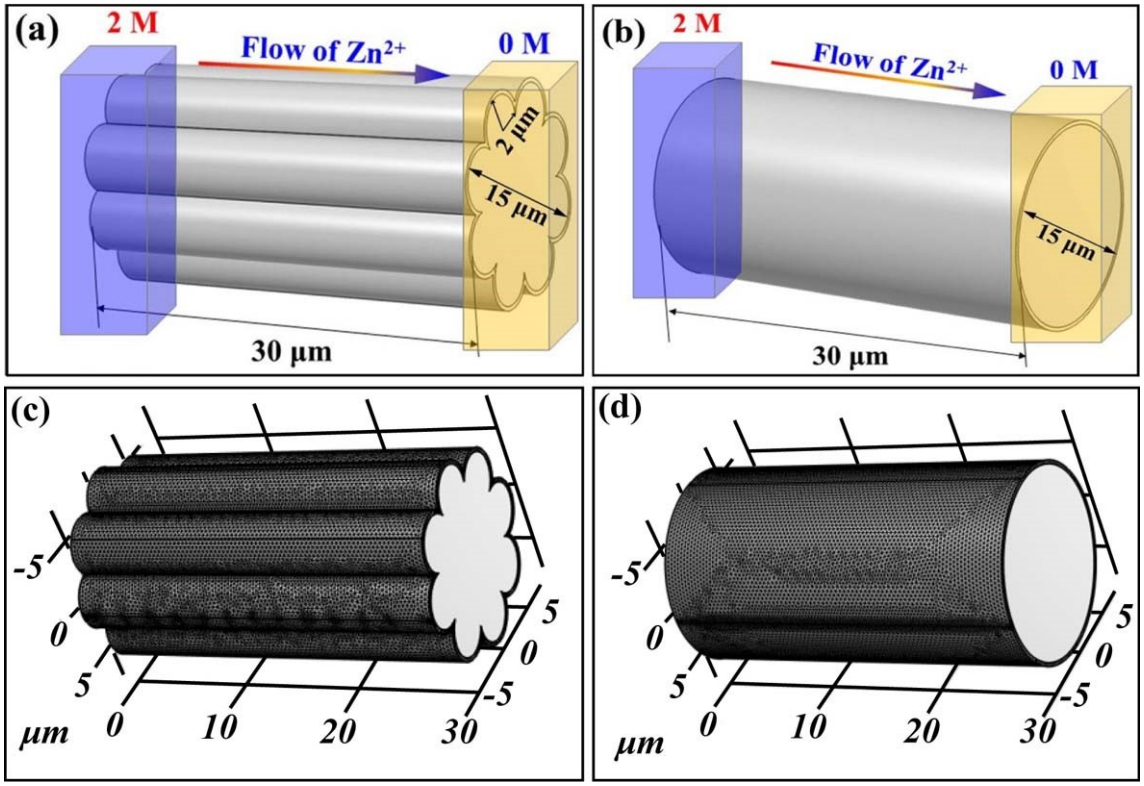

Figure S28. Viscose rayon for VF (a) and cotton fiber for CF (b) with 2 M and 0 M ZnSO4 solution at the left and right sides of systems. The mesh numbers model of VF (c) and CF (d).

7. More details for pore structure of profiled viscose rayon

Figure S29a reveals the surface morphology of profiled viscose rayon, in which the longitudinal grooves and amounts of pores are observed on its surface. Figure S29b represents the surface morphology of the profiled viscose rayon that has been disassembled from a symmetric cell cycled for about 100 h. The profiled viscose rayon has been damaged by an electron beam during SEM characterization, and a crack is found around the damaged area. Therefore, we can observe the internal structure of the profiled viscose rayon from this crack. A large number of nanopores can be observed inside the crack. In addition, profiled viscose rayons are ground by a colloid mill for SEM characterization. The profiled viscose rayons have been torn apart, exposing their interior, where a large number of nanopores can be observed (Figure S29e). This observation is consistent with the structural characteristics of profiled viscose rayons mentioned in various studies.

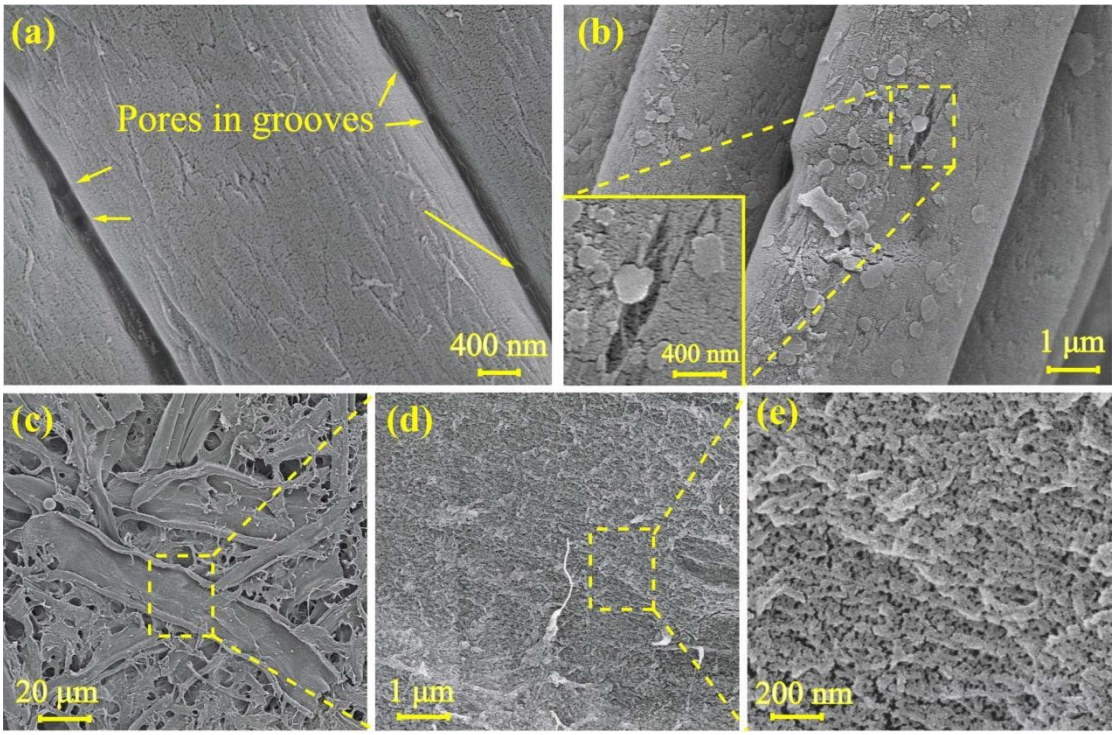

Figure S29. More details about the pore structure of profiled viscose rayon. (a) SEM images of pristine VF, (b) VF disassembled from symmetric cells cycled for about 100 h and (c, d, e) profiled viscose rayon ground with a colloid mill for 3 h.

8. Preparation and characterization of G-VF

25 g of viscose fabric was cut into small pieces (about 2×2 cm^2) and immersed in 1000 g of water for 2 h. Then, the profiled viscose rayons were mechanically ground with a JM-165 colloid mill (Qiangzhong Machinery Technology Co., Ltd., Wenzhou, China) for 3 h to obtain a 2.5% G-VF suspension. 3 g of the suspension was weighed, diluted to 100 g by adding water, and it was fully stirred by using a high-speed blender to ensure that the suspension was well dispersed. Then, the suspension was poured into a glass filter funnel (diameter 4 cm) with a mixed fiber filter membrane (0.45 μm, Haining, China), and the circulating water vacuum pump (Gongyi Yuhua Instrument Co., Ltd.) was started for suction filtration. Finally, the obtained filter cake was hot-pressed and dried at 60 ℃ and 0.1 MPa for 12 h to produce a 60 g/m^2 G-VF separator.

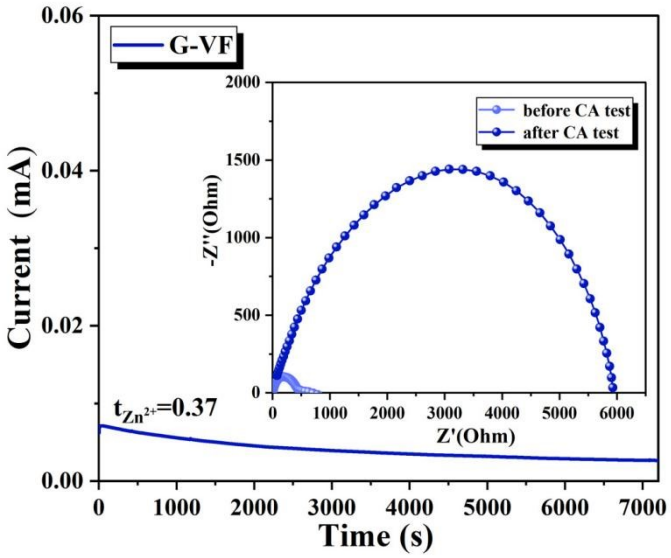

Figure S30. Zn^{2+} transference number of the G-VF separator.

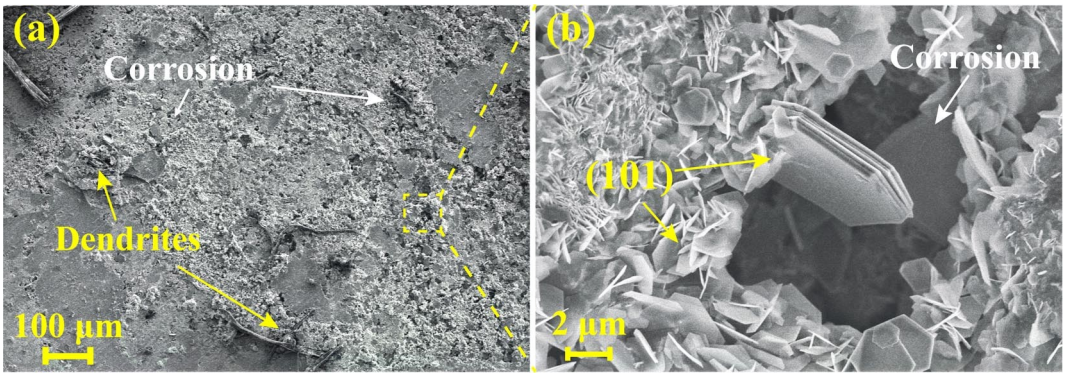

Figure S31. SEM images of Zn anode with G-VF separator cycled for 40 cycles

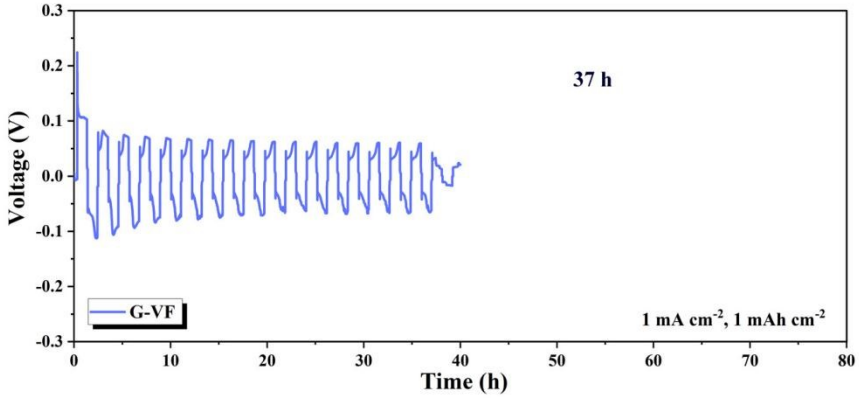

Figure S32. Cycle life of the Zn|G-VF|Zn symmetric cell.

9. Preparation and characterization of VF@SiO_2

Preparation of VF@SiO_2. Briefly, SiO_2 sol was prepared by stöber method.[20] 128 g Ethanol (AR, Xilong, China), 16g tetraethyl orthosilicate (TEOS, AR, Kemiou, China), 2 g deionized water and 3 g aqueous ammonia (AR, Sinophar, China) were mixed and stirred at room temperature (25°C), and a stable SiO_2 sol was obtained after 5 d. Subsequently, the 40×50 mm commercial viscose non-woven fabric was immersed in 0.733 g SiO_2 sol, then sealed and left for 24 h, and finally dried spontaneously to obtain a VF@SiO_2 separator.

Characterization of VF@SiO_2. As VF is immersed in SiO_2 sol, SiO_2 particles are adsorbed on the surface of profiled viscose rayon due to the capillary force generated by the surface grooves of the profiled viscose rayon and hence there is a SiO_2 shell formed on profiled viscose rayon, as shown in Figure S33. To confirm the role of the reservoir-canal structure of profiled viscose rayon, the Zn^{2+} transference number of the Zn|VF@SiO_2|Zn symmetric cell is tested (Figure S34). The result confirms that the surface grooves of the profiled viscose rayon lost their function in accelerating Zn^{2+} transport when they were completely covered. The Zn^{2+} transference number of the cell assembled with VF@SiO_2 separator decreases to 0.43, which would increase the concentration polarization and reduce the cycle life of the cell. In addition, we also assembled a Zn|VF@SiO_2|Zn symmetric cell under the test conditions of 1 mA cm^{-2} and 1 mAh cm^{-2} to explore its cycle life (Figure S35). Cell equipped with VF@SiO_2 separator lost the ultra-long cycle life, and the cycle time was only 60 h. Therefore, it can be concluded that the surface grooves of profiled viscose rayon played a vital role in Zn^{2+} transport and diffusion.

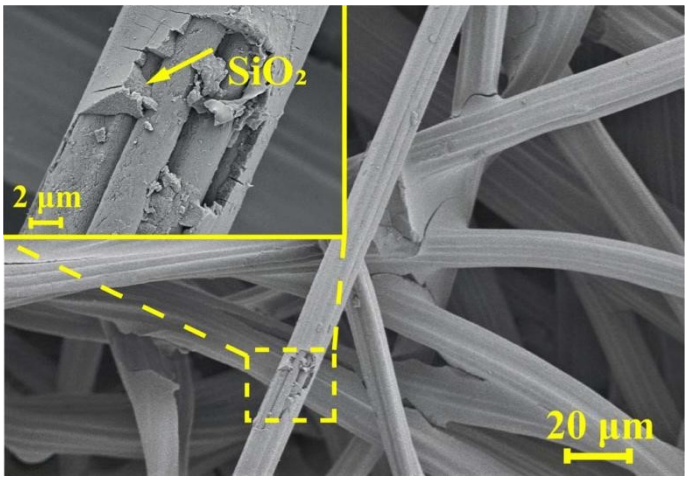

Figure S33. SEM images of the VF@SiO_2 separator

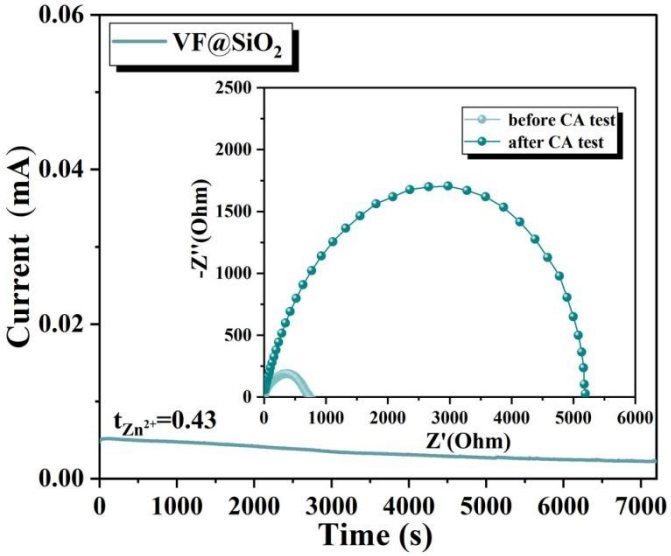

Figure S34. Zn^{2+} transference number of VF@SiO_2 separator.

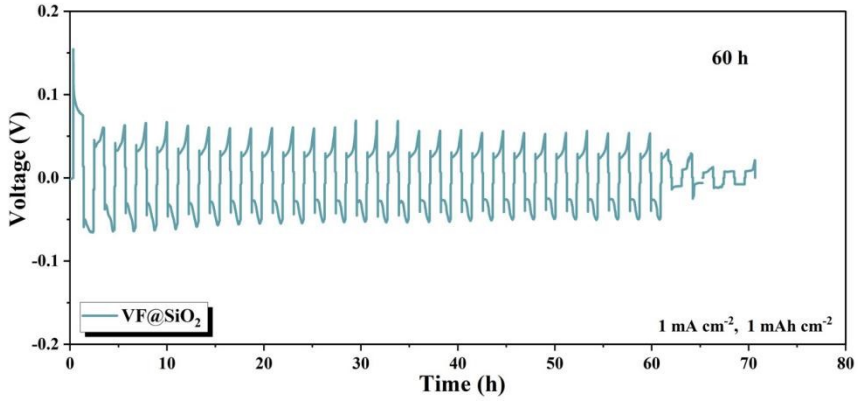

Figure S35. Cycle life of Zn|VF@SiO_2|Zn symmetric cell.

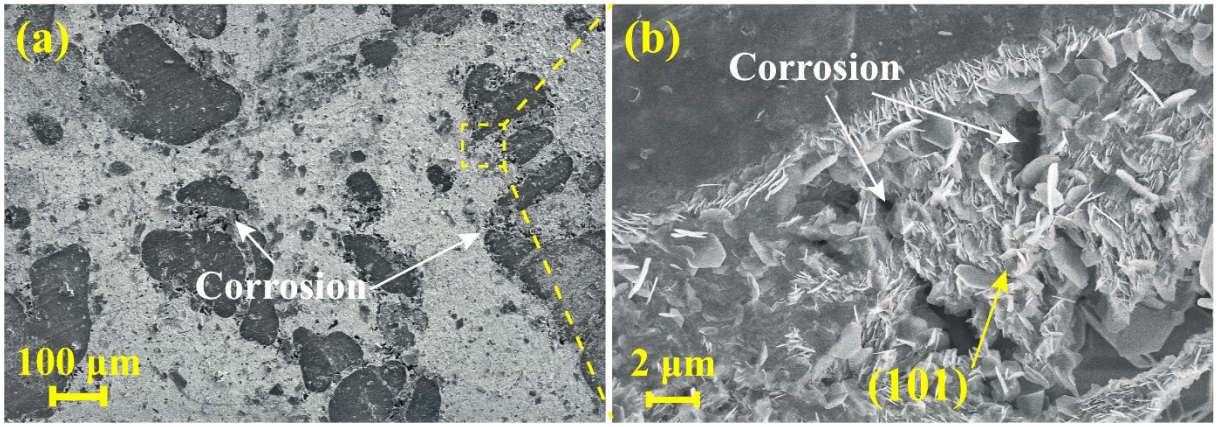

Figure S36. SEM images of Zn anode with VF@SiO_2 separator cycled for 40 cycles.

10. SEM images of Zn crystals growth process

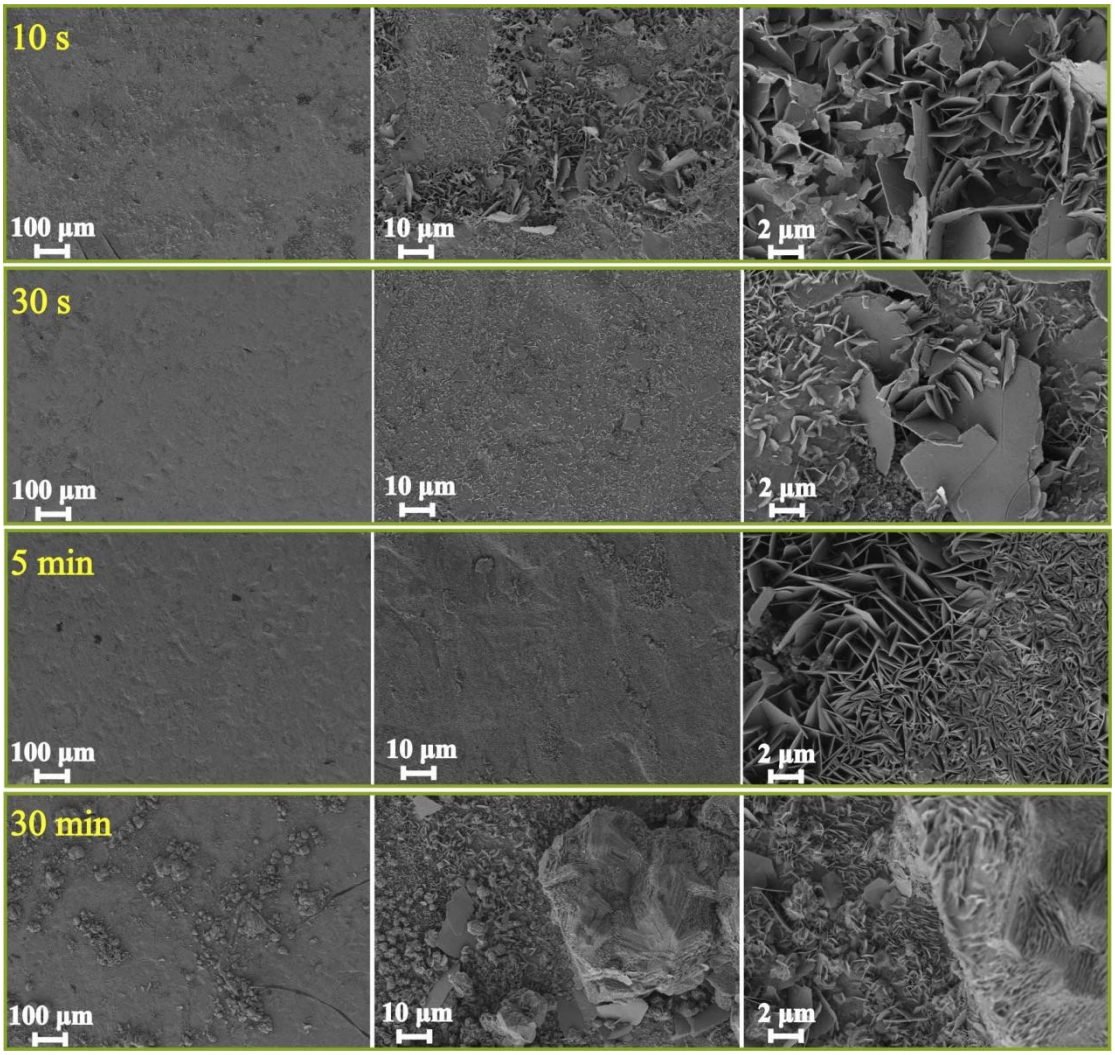

Figure S37. SEM images of Zn crystal growth process on Zn anode of cell with CF separator at different magnifications.

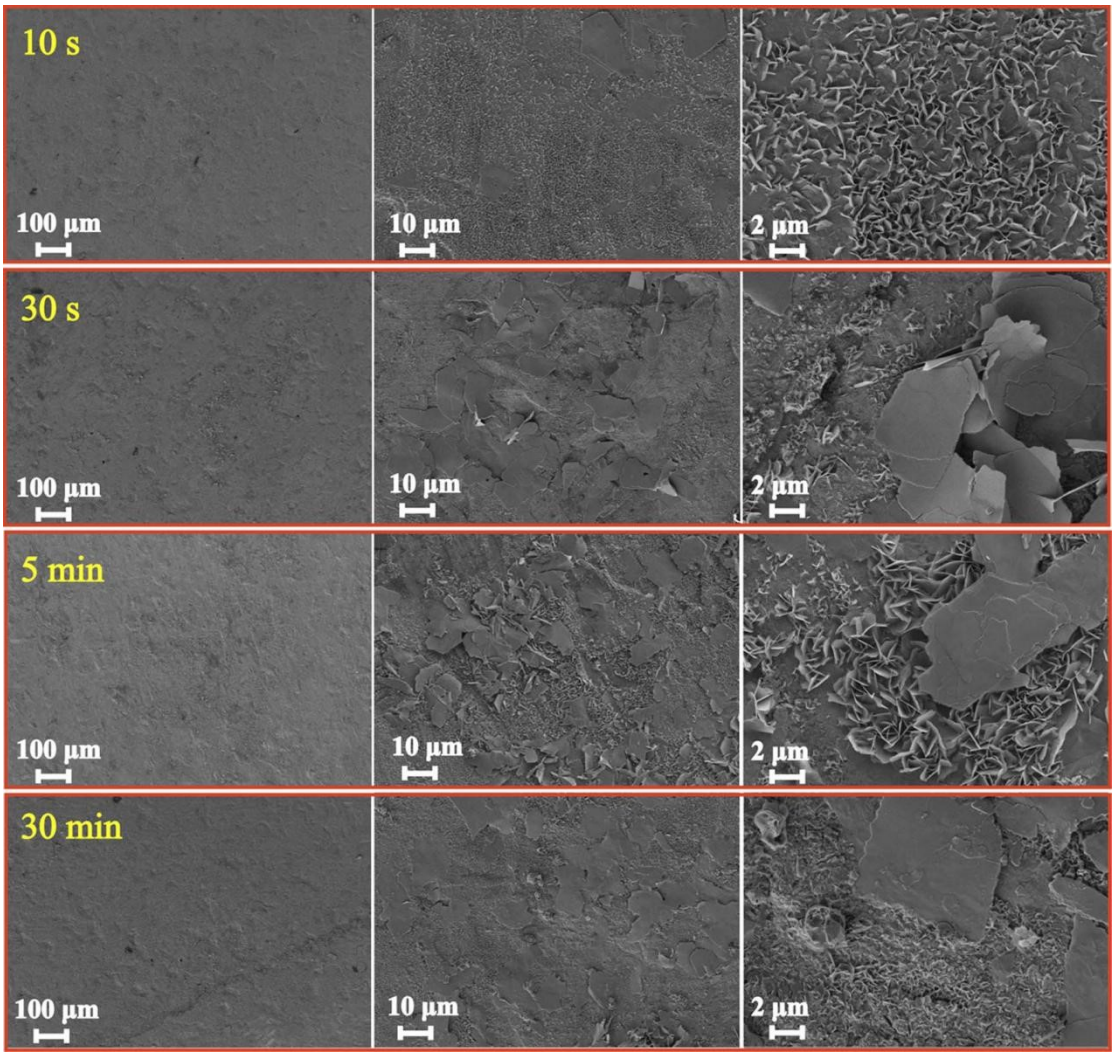

Figure S38. SEM images of Zn crystal growth process on Zn anode of cell with VF separator at different magnifications.

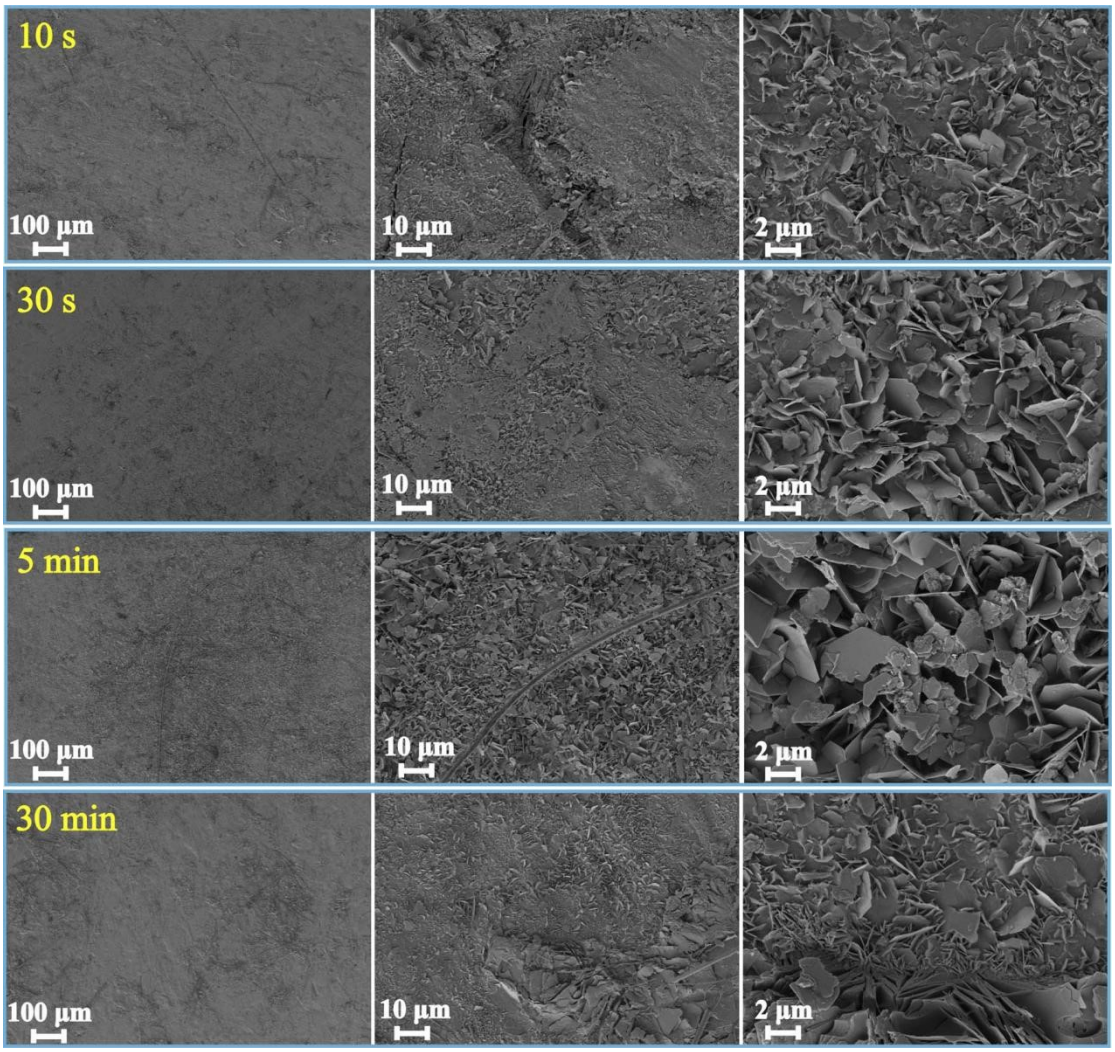

Figure S39. SEM images of Zn crystal growth process on Zn anode of cell with GF separator at different magnifications.

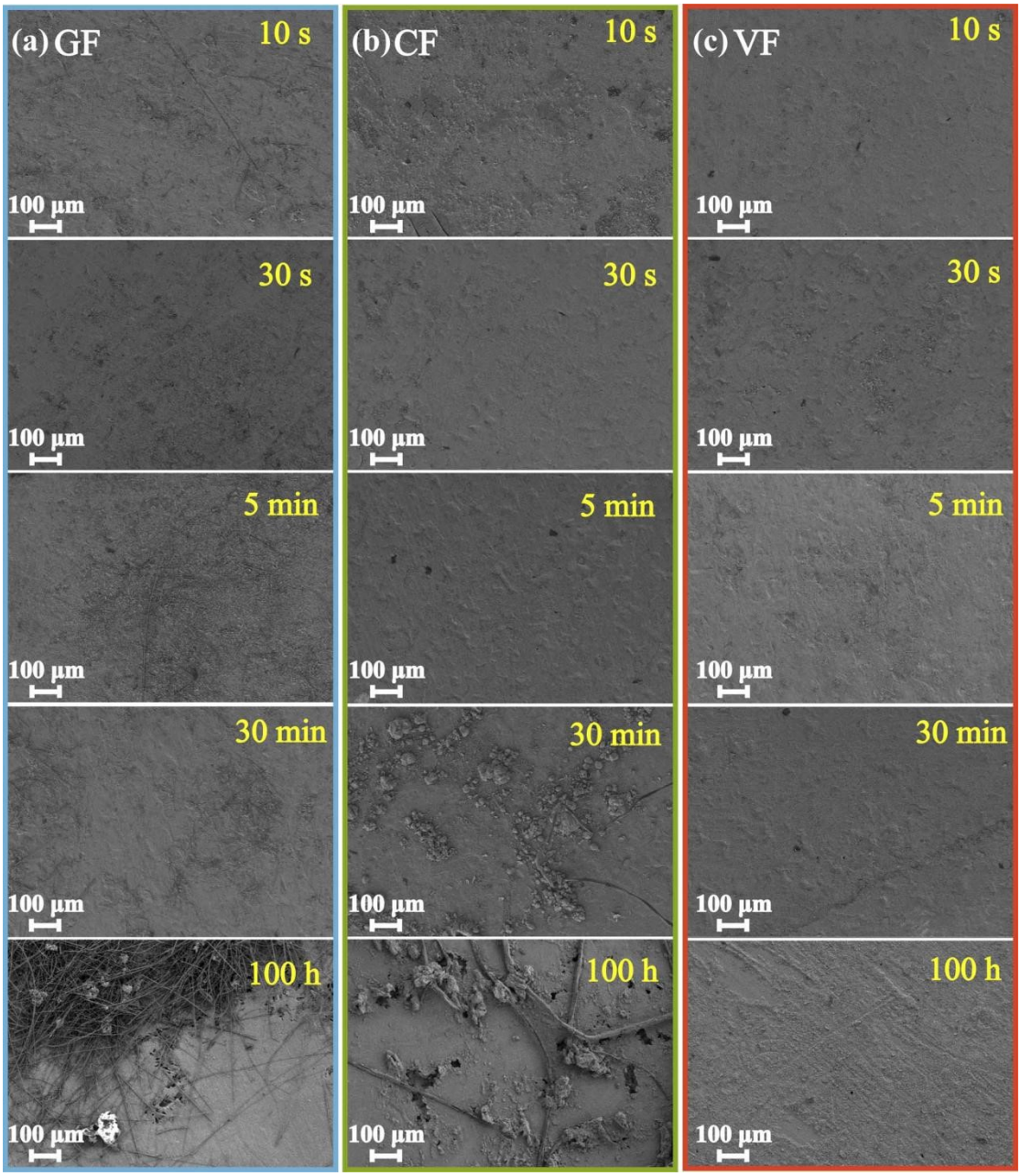

Figure S40. Comparison in the formation of dendrites and HER of cells equipped with GF, CF and VF separators at low magnifications.

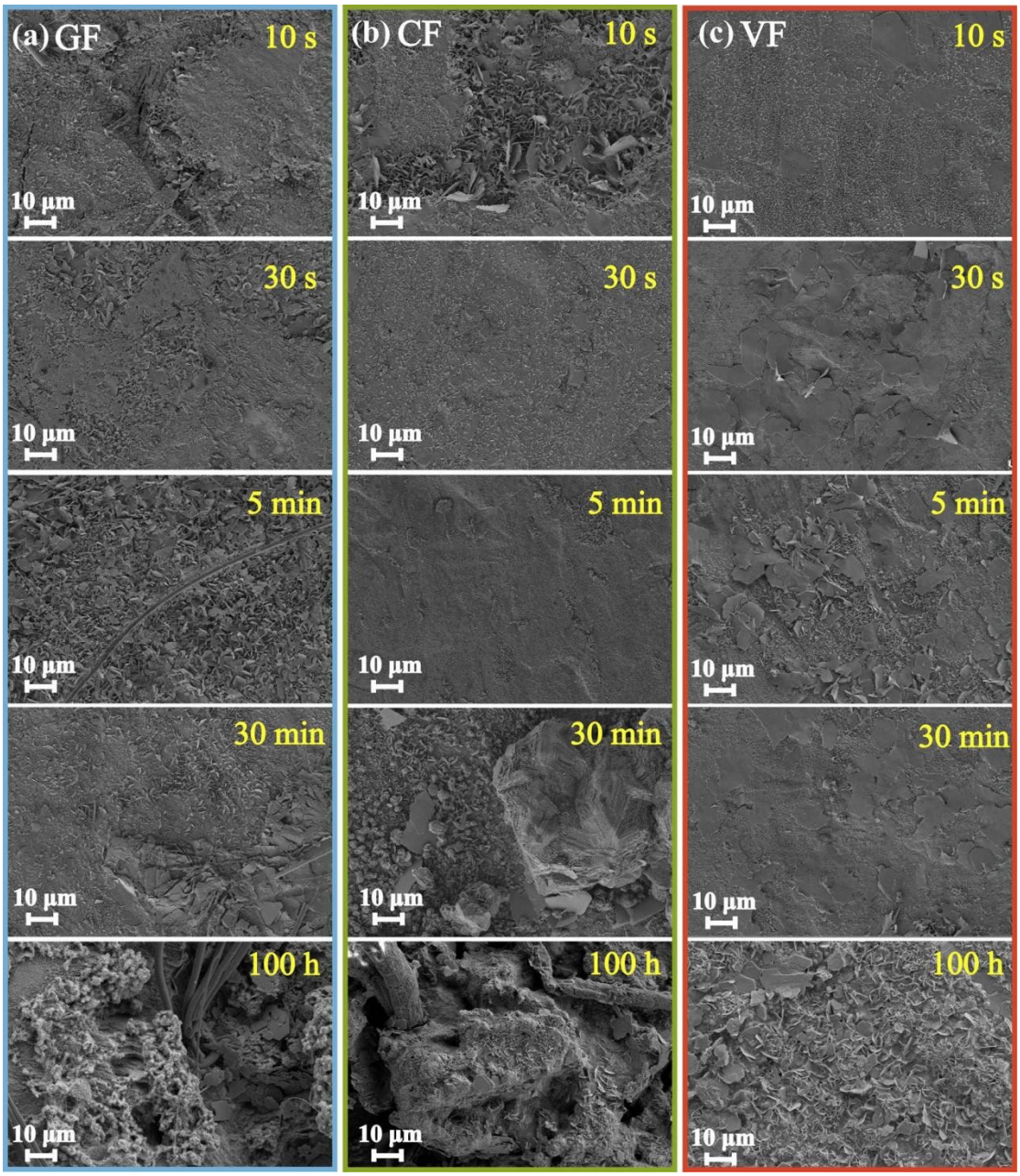

Figure S41. Comparison in the crystals on the cycled Zn anodes of cells equipped with GF, CF and VF separators at high magnifications.

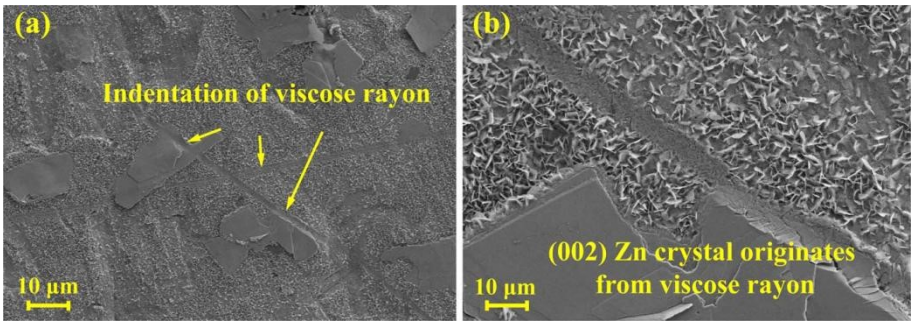

Figure S42. SEM images of (002) Zn crystals originate from viscose rayon.

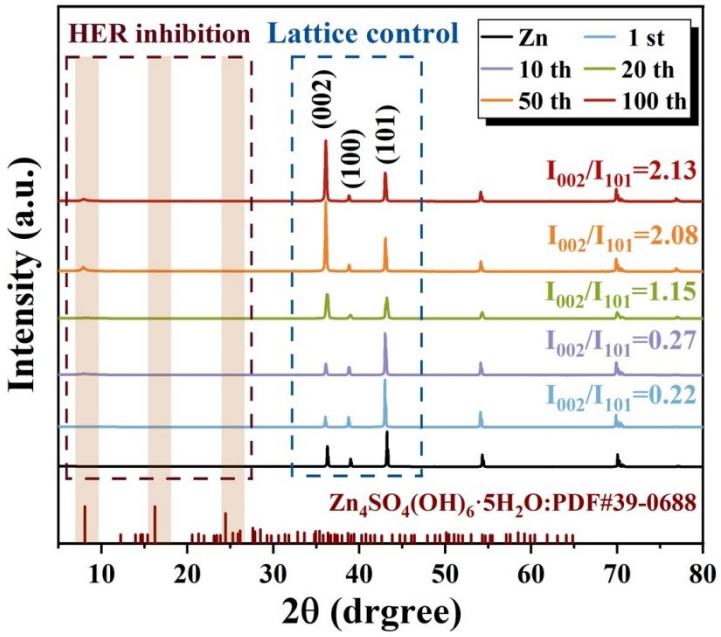

Figure S43. XRD spectra of bare Zn foil and Zn anodes of celled equipped with VF separator after being cycled for different cycles

11. Preparation and characterization of $NH_4V_4O_{10}$

The characterization of $NH_4V_4O_{10}$ prepared by the hydrothermal method was conducted using XRD, with the results shown in Figure S44. It can be observed that the characteristic peaks of $NH_4V_4O_{10}$ perfectly align with the positions of the characteristic peaks in the corresponding standard card PDF#31-0075, indicating that the synthesized $NH_4V_4O_{10}$ is a pure phase crystalline form without any impurities. Concurrently, the prepared cathode sheets are uniform and free of particles, ensuring the stability of the cathode material during battery cycling.

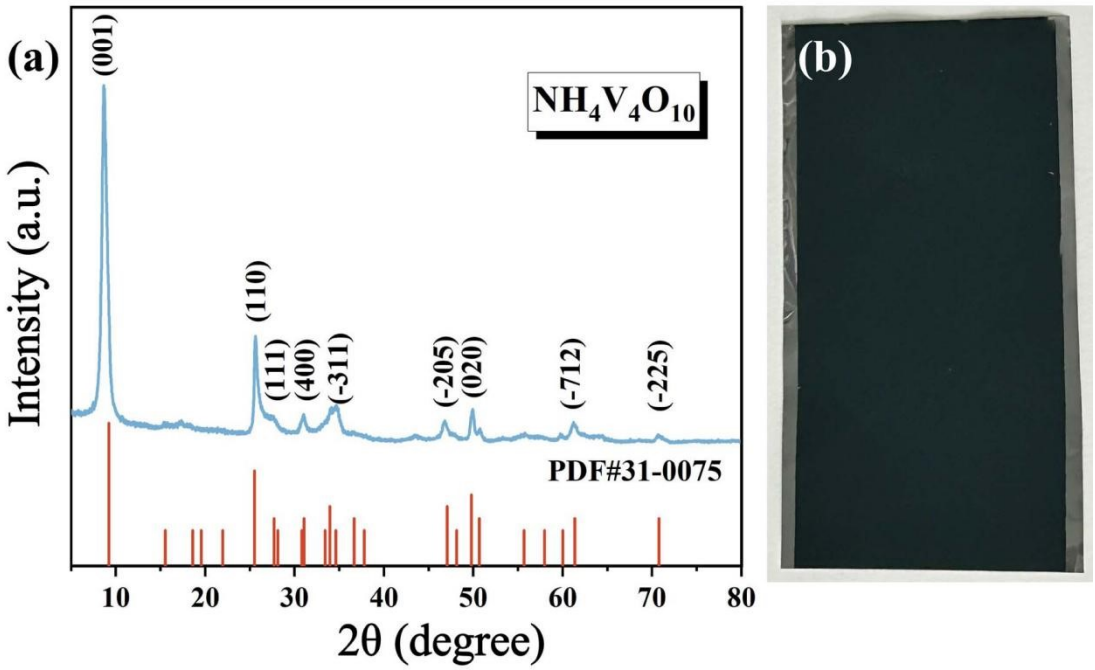

Figure S44. (a) XRD spectrum of the resultant NVO cathode material, and (b) digital photo of the NVO cathode material.

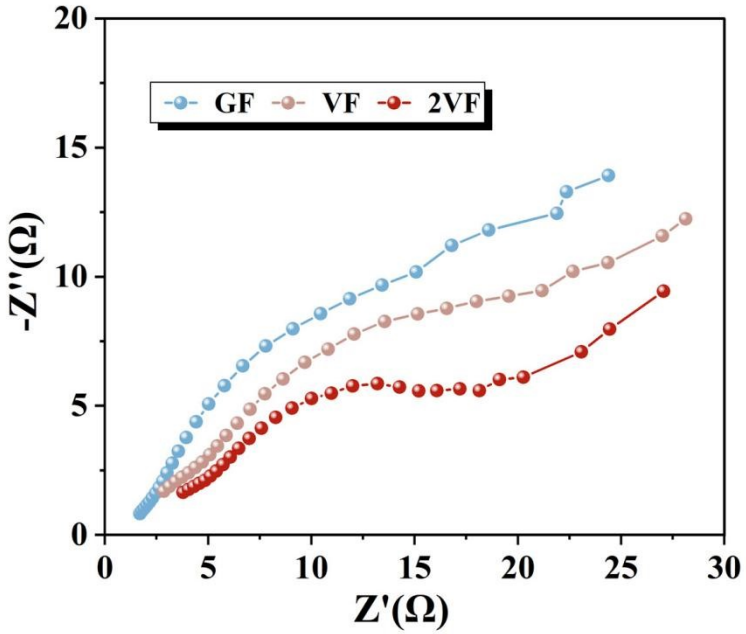

Figure S45. EIS curves of Zn||NVO cell with GF, VF, and 2VF separators.

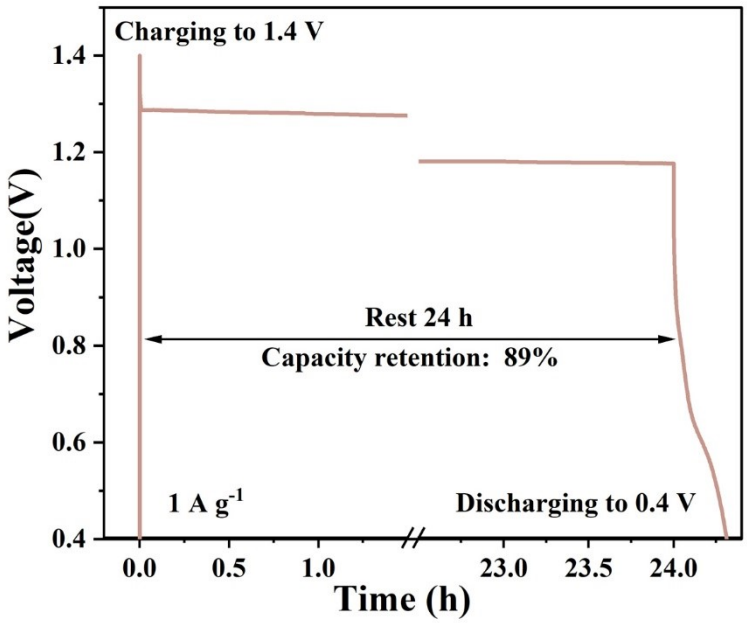

Figure S46. Self-discharge measurements of Zn||NVO full cell with VF separator at 1 A g^{-1}.

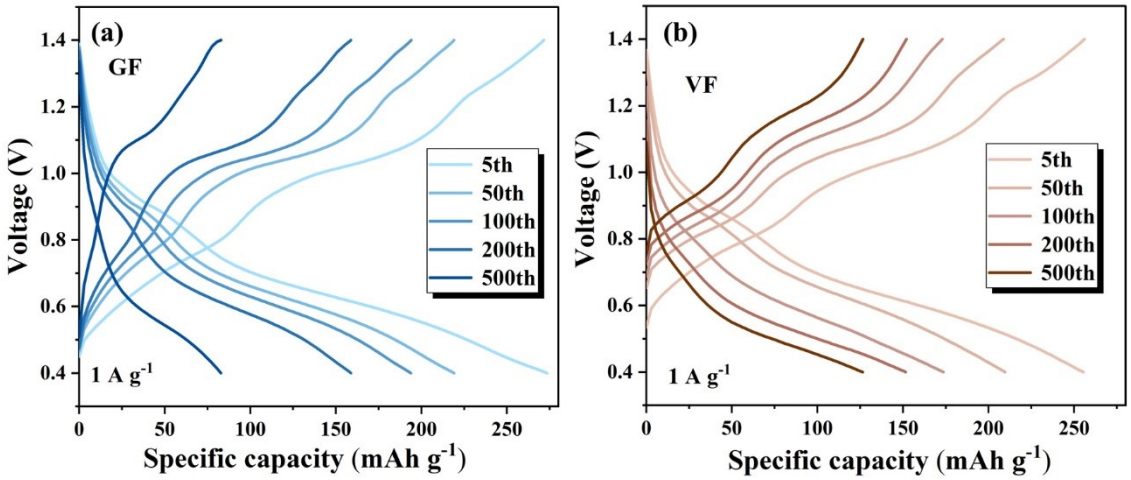

Figure S47. Charge/discharge curves of Zn||NVO full cell with (a) GF and (b) VF separators at 1 A g^{-1}.

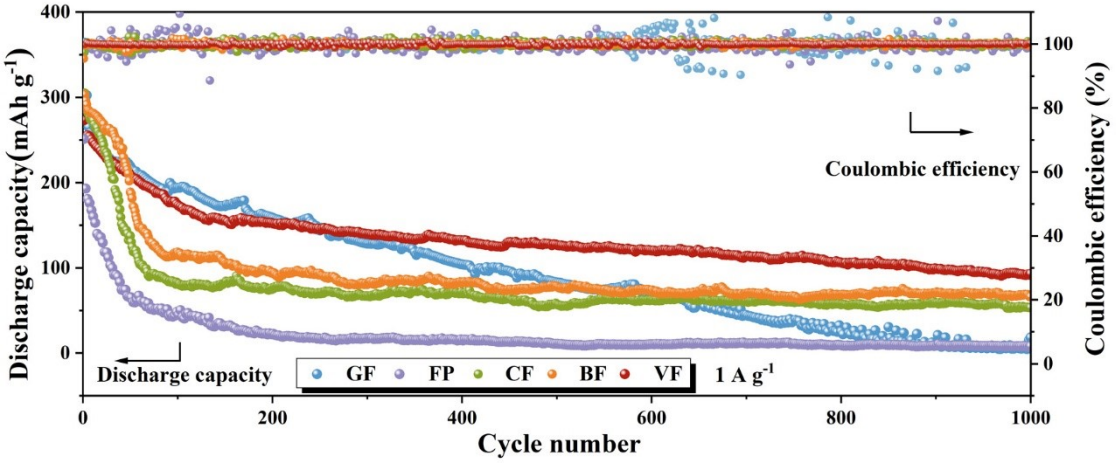

Figure S48. Cycle stability of Zn||NVO full cell with GF, FP, CF, BF and VF separators at 1 A g^{-1}.

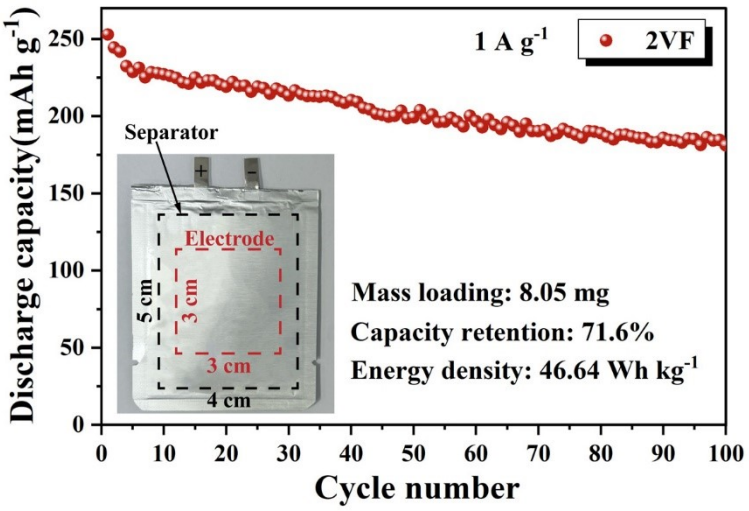

Figure S49. Cycle stability and energy density of pouch cell at 1 A g^{-1}

Supporting References

1. Y. Fang, X. Xie, B. Zhang, Y. Chai, B. Lu, M. Liu, J. Zhou, S. Liang, *Adv. Funct. Mater.* **2022**, *32*, 2109671.
2. J. Cao, D. Zhang, C. Gu, X. Wang, S. Wang, X. Zhang, J. Qin, Z. Wu, *Adv. Energy Mater.* **2021**, *11*, 2101299.
3. Y. Liu, S. Liu, X. Xie, Z. Li, P. Wang, B. Lu, S. Liang, Y. Tang, J. Zhou, *InfoMat* **2023**, *5*, e12374.
4. X. Ge, W. Zhang, F. Song, B. Xie, J. Li, J. Wang, X. Wang, J. Zhao, G. Cui, A*dv. Funct. Mater.* **2022**, *32*, 2200429.
5. W. Zhou, M. Chen, Q. Tian, J. Chen, X. Xu, C. Wong, *Energy Storage Mater.* **2022**, *44*, 57-65.
6. C. Li, Z. Sun, T. Yang, L. Yu, N. Wei, Z. Tian, J. Cai, J. Lv, Y. Shao, M. Rümmeli, J. Sun, Z. Liu, *Adv. Mater.* **2020**, *32*, 2003425.
7. X. Yang, W. Li, J. Lv, G. Sun, Z. Shi, Y. Su, X. Lian, Y. Shao, A. Zhi, X. Tian, X. Bai, Z. Liu, J. Sun, *Nano Res.* **2022**, *15*, 9785-9791.
8. Y. Su, B. Liu, Q. Zhang, J. Peng, C. Wei, S. Li, W. Li, Z. Xue, X. Yang, J. Sun, *Adv. Funct. Mater.* **2022**, *32*, 2204306.
9. T. Liu, J. Hong, J. Wang, Y. Xu, Y. Wang, *Energy Storage Mater.* **2022**, *45*, 1074-1083.
10. F. Wu, F. Du, P. Ruan, G. Cai, Y. Chen, X. Yin, L. Ma, R. Yin, W. Shi, W. Liu, J. Zhou, X. Cao, *J. Mater. Chem. A* **2023**, *11*, 11254-11263.
11. N. Maeboonruan, J. Lohitkarn, C. Poochai, T. Lomas, A. Wisitsoraat, S. Kheawhom, S. Siwamogsatham, A. Tuantranont, C. Sriprachuabwong, *J. Sci. Adv. Mater. Dev.* **2022**, *7*, 100467.
12. Y. Qin, P. Liu, Q. Zhang, Q. Wang, D. Sun, Y. Tang, Y. Ren, H. Wang, *Small* **2020**, *16*, 2003106.
13. Y. Guo, W. Cai, Y. Lin, Y. Zhang, S. Luo, K. Huang, H. Wu, Y. Zhang, *Energy Storage Mater.* **2022**, *50*, 580-588.
14. S. Yang, Y. Zhang, Y. Zhang, J. Deng, N. Chen, S. Xie, Y. Ma, Z. Wang, *Adv. Funct. Mater.* **2023**, *33*, 2304280.
15. Y. Li, X. Peng, X. Li, L. Dong, F. Kang, *Adv. Mater.* **2023**, *35*, 2300019.
16. Y. Zhang, Z. Liu, X. Li, L. Fan, Y. Shuai, N. Zhang, *Adv. Energy Mater.* **2023**, *13*, 2302126.
17. J. Cao, D. Zhang, C. Gu, X. Zhang, M. Okhawilai, S. Wang, J. Han, J. Qin, Y. Huang, *Nano Energy* **2021**, *89*, 106322.

18. P. Cao, H. Zhou, X. Zhou, Q. Du, J. Tang, J. Yang, *ACS Sustainable Chem. Eng.* **2022**, *10*, 8350-8359.
19. T. Saito, I. Shibata, A. Isogai, N. Suguri, N. Sumikawa, Carbohydr. Polym. **2005**, 61, 414-419.
20. X. Zhang, S. Cai, D. You, L. Yan, H. Lv, X. Yuan, B. Jiang, *Adv. Funct. Mater.* **2013**, *23*, 4361-4365.